

Harnessing elastic anisotropy to achieve low-modulus refractory high-entropy alloys for biomedical applications

Stephan Schönecker^a, Xiaojie Li^{b,*}, Daixiu Wei^{c,*}, Shogo Nozaki^d, Hidemi Kato^c, Levente Vitos^{a,e,f}, Xiaoping Li^{a,*}

^a Unit of Properties, Department of Materials Science and Engineering, KTH Royal Institute of Technology, Stockholm SE-10044, Sweden

^b Department of Physics, Taizhou University, Taizhou 318000, Zhejiang, China

^c Institute for Materials Research, Tohoku University, 2-1-1 Katahira, Sendai, Miyagi 980-8577, Japan

^d Department of Materials Science, Tohoku University, 6-6-02 Aramaki Aza Aoba, Sendai, Miyagi 980-8579, Sendai, Japan

^e Research Institute for Solid State Physics and Optics, Wigner Research Center for Physics, Budapest H-1525, P.O. Box 49, Hungary

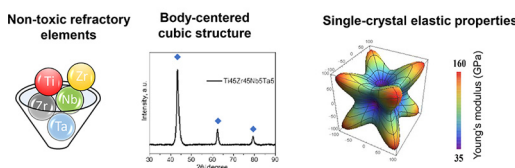
^f Department of Physics and Astronomy, Division of Materials Theory, Uppsala University, Box 516, SE-75120 Uppsala, Sweden

HIGHLIGHTS

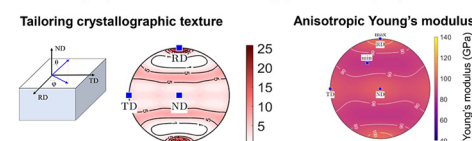
- Systematic calculation of elastic properties in Ti-containing, biocompatible refractory high-entropy alloys.
- Modeling of non-random texture effects on poly-crystalline moduli.
- Directionally preferential Young's moduli achievable in single crystals and textured poly-crystals.
- Valence electron count has a dominant influence on elastic anisotropy.

GRAPHICAL ABSTRACT

Multi-principal element alloy design idea for biocompatible implants



Polycrystals with directionally preferential properties



ARTICLE INFO

Article history:

Received 6 October 2021

Revised 17 December 2021

Accepted 27 January 2022

Available online 01 February 2022

Keywords:

Refractory high-entropy alloy

Young's modulus

Elastic anisotropy

Crystallographic texture

Density-functional theory

ABSTRACT

A high-priority target in the design of new metallic materials for load-bearing implant applications is the reduction of Young's modulus approximating that of cortical bone in the predominant loading direction. Here, we explore how directionally preferential bulk elastic properties of implant materials are achieved by harnessing elastic anisotropy. Specifically focusing on recently proposed biocompatible refractory high-entropy alloys (RHEAs) in the body-centered cubic structure, we conduct systematic density-functional theory calculations to investigate the single-crystal elastic properties of 21 Ti-containing RHEAs. Our results provide evidence that the valence electron count has a dominant influence on elastic anisotropy and crystal directions of low Young's modulus and high torsion modulus in the RHEAs. By means of modeling the orientation distribution function for crystallographic texture, we examine the effect of non-random texture on the anisotropic poly-crystalline Young's modulus and torsion modulus with varying texture sharpness. We adopt fiber textures that can result from rolling and distinct texture orientations that can form during rapid directional solidification. We discuss the potential for lowering

Abbreviations: RHEA, refractory high-entropy alloy; ODF, orientation distribution function; DFT, density-functional theory; SLM, selective laser melting; VEC, valence electron count.

* Corresponding authors.

E-mail addresses: lixj26@tzc.edu.cn (X. Li), wei1987xiu@imr.tohoku.ac.jp (D. Wei), xiaoqli@kth.se (X. Li).

<https://doi.org/10.1016/j.matdes.2022.110430>

0264-1275/© 2022 The Authors. Published by Elsevier Ltd.

This is an open access article under the CC BY license (<http://creativecommons.org/licenses/by/4.0/>).

Young's modulus in the RHEAs by using single crystals or textured aggregates. Furthermore, we prepare four of the theoretically considered alloys by arc-melting and report their lattice parameters, quasi-isotropic Young's moduli, and Wickers hardnesses.

© 2022 The Authors. Published by Elsevier Ltd. This is an open access article under the CC BY license (<http://creativecommons.org/licenses/by/4.0/>).

1. Introduction

Metallic materials used in biomedical load-bearing applications, e.g., hip replacements and artificial knee joints, should possess good biocompatibility and corrosion stability in the human body, high fatigue resistance and hardness, high strength-to-weight ratio, good ductility, low Young's modulus, excellent wear resistance, and be composed of non-toxic and hypoallergenic elements [1–4]. A low Young's modulus of the bone-replacing implant is an important constraint as a significant stiffness mismatch to the host bone can induce bone resorption owing to stress shielding, which may result in implant loosening and cause periprosthetic fracture [5]. The poly-crystal Young's moduli of the most commonly used surgical materials including 316L stainless steel, Co-Cr-Mo alloys, and Ti-6wt.%Al-4wt.%V alloy (Ti64) are much higher (110–240 GPa [6]) than human cortical bone (15–20 GPa; long-bone direction [7,8]). Besides, these alloys contain one or several cytotoxic elements (Ni, Cr, Co, and V), which can be released into the tissues surrounding the implant as a consequence of corrosion in the hostile body environment and result in undesirable medical effects. Thus, developing new, non-toxic metallic biomaterials that meet the above biomechanical constraints has significant merit.

The potential of refractory high-entropy alloys (RHEAs) as novel implant material has been recognized recently [9–18]. Biocompatible RHEAs use concentrated mixtures of many, primary refractory elements as an alloy base, i.e., elements like Ti, Nb, Ta, and Zr that also show high biocompatibility and low cytotoxicity [19,20]. In particular the Ti-Zr-Nb-Mo-Ta alloy base was in the focus of most of these previous alloy studies, and some compositions show *in vitro* biocompatibility comparable to or better than clinically used 316L stainless steel, commercially pure Ti, and Ti64, as well as exceptional mechanical strength (i.e., 0.2% proof stress > 1000 MPa) [9,10,12–16]. Lesser attention has been paid to the elastic properties of biocompatible RHEAs [13,14]. While these previous results showcase the potential of biocompatible RHEAs, these materials are at an early stage of development and improved properties in terms of biocompatibility, mechanical properties, wear and corrosion resistance, etc. are expected. Compositional complexity of RHEAs is, however, a severe challenge to experimental alloy screening and limits quantitative and well-targeted design.

Bone stiffness-matching in load-bearing applications primarily refers to the long-bone (longitudinal) direction, as leg bones receive the predominant loads in this direction under common activities such as walking, running, and stair climbing. Such anisotropic loading pattern motivates a departure from an isoelastic bulk implant towards the design of prostheses that possess low Young's modulus in the predominant loading direction. This can be achieved by harnessing elastic anisotropy of materials. On the one hand, nearly all single crystals are elastically anisotropic. Thus, in a single-crystal material there are crystal directions with Young's modulus values that are lower than the quasi-isotropic Young's modulus of a poly-crystalline aggregate of that material. Following this concept, low-modulus single-crystal implants made of β -type Ti alloys were proposed [21,22]. Single crystals of multi-component alloys are, however, difficult to grow and their machining is challenging. On the other hand, a non-random, crystallographically textured distribution of grains in a poly-crystalline

material can have profound influences on many macroscopic properties [23,24] and may be exploited to design materials with directionally preferential elastic properties.

In this paper, using first-principles simulations, we first systematically investigate the single-crystal elastic properties of 21 RHEAs, 18 of which were recently shown to exhibit the body-centered cubic (bcc) phase. Using a scale-jumping approach, we then calculate the elastic moduli of poly-crystalline single-phase aggregates of these alloys. We adopt both random and non-random crystallographically textured distributions of grains. The simulated non-random grain distributions are associated with fiber textures, which can form during rolling, and a microstructure with distinct texture orientations, which can develop by rapid directional solidification during, for instance, selective laser melting (SLM). Furthermore, four of the 21 RHEAs were prepared by arc melting and their lattice parameters, Young's moduli, and hardnesses determined. The present theoretical and experimental study provides knowledge on mechanical properties of RHEAs that are of immediate relevance for the final product design and, thus, may guide the further development of low-modulus RHEAs.

2. Theory and method

2.1. Elastic properties of cubic single crystals

Let S_{ijkl} and $C_{ijkl} = S_{ijkl}^{-1}$ be the compliance tensor and the stiffness tensor, respectively, of a linear elastic single crystal. Each Cartesian index runs over 1, 2, and 3. Both four-rank tensors are expressed in the crystal coordinate system defined by the orthonormal set of axes x_i . For crystals of cubic symmetry, considered in this work, there are three independent compliances, i.e. S_{1111} , S_{1122} , and S_{2323} . These are commonly written S_{11} , S_{12} , and S_{44} using contracted double subscript notation, and similar notation is used for the elastic constants C_{ij} . Both full and contracted notations are used interchangeably below as needed.

Single crystals of cubic symmetry are intrinsically elastically anisotropic, except when the elastic coefficients fulfill the isotropy condition,

$$2S_{11} - 2S_{12} - S_{44} = 0, \quad (1)$$

or, equivalently, $C_{11} - C_{12} - 2C_{44} = 0$. Several anisotropic elastic properties describe single crystals and are derived from S_{ijkl} . In the present work, we characterize materials by their Young's modulus E , i.e., the stiffness under uniaxial load, and their torsion modulus T (or rigidity modulus), describing shear resistance under applied torque. We examine the case where torque around a torque axis refers to shear in directions perpendicular to this axis.

The magnitudes of E and T vary with direction of applied stress and direction of torque axis, respectively. The direction dependences of E and T are governed by tensor transformation laws of S_{ijkl} [25],

$$S'_{ijkl} = \alpha_{im} \alpha_{jn} \alpha_{ko} \alpha_{lp} S_{mnop}, \quad (2)$$

to another set of orthogonal axes x'_i with the same origin (i.e., a rotation). The α_{ij} are the direction cosines of angle between axes x'_i with respect to x_j . If, without loss of generality, the new x'_3 axis is placed

in the direction of a unit vector \mathbf{n} , one obtains for Young's modulus in this direction, [26]

$$E(\mathbf{n})^{-1} = S'_{33} = S_{11} - (2S_{11} - 2S_{12} - S_{44})N^4, \quad (3)$$

where

$$N^4 = n_1^2 n_2^2 + n_1^2 n_3^2 + n_2^2 n_3^2. \quad (4)$$

The components $n_i \equiv \alpha_{3i}$ are the direction cosines of x'_3 with respect to the crystal coordinate system. The direction dependent torsion modulus T is obtained by placing, without loss of generality, the new axis x'_3 parallel to the normal of the plane of shear coinciding with the torque axis \mathbf{n} , and the new axes x'_1 and x'_2 parallel to the directions of shear. Then, for a specimen of circular cross-section [26,27],

$$\begin{aligned} T(\mathbf{n})^{-1} &= (S'_{44} + S'_{55})/2 \\ &= S_{44} + 2(2S_{11} - 2S_{12} - S_{44})N^4. \end{aligned} \quad (5)$$

T in this definition depends only on the direction defining the torque axis and not on the perpendicular directions where shears are applied. E and T can thus be represented by a single surface in three dimensions. For convenience, we also specify \mathbf{n} by a crystal direction $[hkl]$ and use the notation $E([hkl])$ or $T([hkl])$, in which case $n_1 = h/(h^2 + k^2 + l^2)^{1/2}$ and similar for n_2 and n_3 . To denote equivalent directions, we use $E(\langle hkl \rangle)$ or $T(\langle hkl \rangle)$.

To measure the elastic anisotropy of single crystals, we employ the universal anisotropy index $A_u \geq 0$ [28]. This measure applies to any crystal class and can be used to characterize the elastic anisotropy of textured specimens as their averaged elastic properties can be represented by effective stiffness (compliance) tensors, see below.

2.2. Elastic properties of poly-crystalline, textured, one-phase materials from an orientation distribution function

We consider macroscopically large, poly-crystalline, one-component materials composed of a large number of crystallites (grains). The objective is the determination of elastic properties of poly-crystal samples from the individual crystallites and crystallographic texture characterizing the poly-crystalline materials. The crystallographic texture information is provided by an orientation distribution function (ODF). In the present case, the ODF results from modeling, but it may be obtained from pole figure inversion or electron backscatter diffraction data.

Let g be an orientation, i.e., a rotation that translates the sample coordinate system onto the crystal coordinate system, and $f(g)$ the sample ODF describing the relative frequency of crystal orientations by volume [29]. Let further $S_{ijkl}^S(g)$ and $C_{ijkl}^S(g)$ be the compliance tensor and the stiffness tensor, respectively, of a crystallite in the sample (S) coordinate system, denoted x_i^S . Both four-rank tensors depend on g since the orientation is, in principle, different in each grain. $S_{ijkl}^S(g)$ and $C_{ijkl}^S(g)$ are transformed to S_{ijkl} and C_{ijkl} , respectively, and vice versa, by means of Eq. (2).

Elastic loading of a poly-crystalline material induces inhomogeneous stress and strain distributions, as the compliance $S_{ijkl}^S(g)$ varies from grain to grain. In order to determine the macroscopic or effective elastic properties of poly-crystalline, one-component aggregates, simplifying assumptions and averaging are frequently used. The Voigt model assumes that the induced strain field is homogeneous throughout the sample and equals the macroscopically induced strain. The Voigt average of the compliance tensor given an ODF f is defined by an weighted integration over all elements of orientation [30],

$$\langle S_{ijkl}^S \rangle^{\text{Voigt}} = \left[\int_{\text{SO}(3)} C_{ijkl}^S(g) f(g) dg \right]^{-1}. \quad (6)$$

The Reuss model assumes that the applied stress field is homogeneous throughout the sample and equals the macroscopically applied stress. The Reuss average is given by the integral

$$\langle S_{ijkl}^S \rangle^{\text{Reuss}} = \int_{\text{SO}(3)} S_{ijkl}^S(g) f(g) dg. \quad (7)$$

Measured stiffness tensors of aggregates lie, in general, between the Voigt and Reuss average bounds, and in practice one frequently uses their arithmetic mean,

$$\langle S_{ijkl}^S \rangle^{\text{Hill}} = \frac{\langle S_{ijkl}^S \rangle^{\text{Voigt}} + \langle S_{ijkl}^S \rangle^{\text{Reuss}}}{2}, \quad (8)$$

known as the Hill average. The following Eqs. (9)–(13) apply to either averaging scheme (Voigt, Reuss, or Hill), and we drop the related superscript in the following.

Anisotropic elastic properties of a poly-crystalline sample derived from its effective $\langle S_{ijkl}^S \rangle$ tensor include Young's modulus and torsion modulus. Determination of their direction dependences follows the same principle as outlined above, with the difference that the axes transformation is from x_i^S to new axes $x_i^{S'}$. Young's modulus in a general direction of applied uniaxial stress \mathbf{n} is given by [31]

$$\langle E^S \rangle(\mathbf{n}) = \left(\langle S_{ijkl}^S \rangle n_i n_j n_k n_l \right)^{-1}, \quad (9)$$

where the n_i are the direction cosines of $x_3^{S'}$ with respect to the axes in the sample coordinate system. To obtain the torsion modulus, we first note that the shear modulus varies with shear plane and shear direction. Choosing without loss of generality the new axis $x_3^{S'}$ parallel to the normal of the shear plane \mathbf{n} and the new axis $x_2^{S'}$ parallel to the direction of shear \mathbf{u} , but orthogonal to \mathbf{n} , the shear modulus is given by [31]

$$\langle G^S \rangle(\mathbf{n}, \mathbf{u}) = \left(4 \langle S_{ijkl}^S \rangle n_i u_j n_k u_l \right)^{-1}, \quad (10)$$

where the $u_i \equiv \alpha_{2i}$ are the direction cosines of $x_2^{S'}$ with respect to the sample coordinate system. Noting that the second direction of applied shear \mathbf{p} is perpendicular to both \mathbf{n} and \mathbf{u} [cf. Eq. (5)], for the torsion modulus follows,

$$\langle T^S \rangle(\mathbf{n}, \mathbf{u}) = \left(2 \langle S_{ijkl}^S \rangle (n_i u_j n_k u_l + n_i p_j n_k p_l) \right)^{-1}. \quad (11)$$

The $p_i \equiv \alpha_{1i}$ are the direction cosines of $x_1^{S'}$ with respect to the sample coordinate system. In contrast to the single-crystal counterpart in Eq. (5), $\langle T^S \rangle(\mathbf{n}, \mathbf{u})$ in poly-crystals depends on the direction of applied shear. In this paper, we determine the torsion modulus average across all directions of applied shear within the shear plane and denote the torsion modulus by $\overline{\langle T^S \rangle}(\mathbf{n})$. For convenience and displaying purposes, we specify the direction dependences of Young's modulus and torsion modulus by spherical angles θ and ϕ and use the notation $\langle E^S \rangle(\theta, \phi)$ or $\overline{\langle T^S \rangle}(\theta, \phi)$. θ and ϕ are defined with introducing the sample coordinate system in Section 3.

The effective tensors have symmetry properties that are typically different from those of the crystallites composing the poly-crystal, depending on crystallographic texture. Simplifying the sums on the right hand sides of Eqs. (9) and (10) is possible if the symmetry properties of $\langle S_{ijkl}^S \rangle$ are known. For poly-crystalline, statistically isotropic and homogeneous aggregates,

$f(g) = 1$ and the effective compliance tensor, assuming cubic crystallites, is given by

$$\langle S_{ijkl}^S \rangle = \left(\Lambda_{iso}^S \delta_{ij} \delta_{kl} + G_{iso}^S (\delta_{ik} \delta_{jl} + \delta_{ij} \delta_{kl}) \right)^{-1}, \quad (12)$$

where

$$\Lambda_{iso}^S = \frac{G_{iso}^S (E_{iso}^S - 2G_{iso}^S)}{3G_{iso}^S - E_{iso}^S} \quad (13)$$

and δ_{ij} denotes the Kronecker delta. The Young modulus E_{iso}^S and the shear modulus $G_{iso}^S = T_{iso}^S$ are independent on direction. The bulk modulus $B_{iso}^S = G_{iso}^S E_{iso}^S / (9G_{iso}^S - 3E_{iso}^S)$. Explicit equations for the Voigt-Reuss-Hill averages of G_{iso}^S and B_{iso}^S in terms of C_{11} , C_{12} , and C_{44} can be found in Ref. [32].

2.3. Density-functional theory calculations

Density-functional theory (DFT) calculations were performed to determine C_{11} , C_{12} , and C_{44} for various alloys in the bcc structure. In practice, C_{11} and C_{12} were obtained from the single-crystal bulk modulus $B = (C_{11} + 2C_{12})/3$ and tetragonal shear modulus $C' = (C_{11} - C_{12})/2$. The bulk modulus was determined from an exponential Morse-type function fitted to computed total energies [33]. Volume-conserving orthorhombic and monoclinic deformations were applied to determine C' and C_{44} , respectively, as previously described in Ref. [34]. All theoretical moduli of polycrystalline aggregates reported in this paper were obtained by means of Hill averaging using the MTEX 5.4 software [35,36].

Our DFT calculations were performed with the exact muffin-tin orbitals method [37,38]. The local-density approximation [39] was employed to describe exchange and correlation and the total energy was computed via the full charge-density technique [40–42]. Chemical randomness in the RHEAs was described within the coherent-potential approximation [40–42]. Brillouin zone integrations were performed on a $33 \times 33 \times 33$ uniform k mesh. The Green's function was calculated for 16 complex energy points at the valence states below the Fermi level. We included s, p, d, and f orbitals in the basis set.

2.4. Sample fabrication, measurements of Young's modulus and hardness

Four of the 21 theoretically considered RHEAs (complete list in Table 3) were selected for synthesis and determination of phase constitution, lattice parameter, Young's modulus, and hardness. The nominal compositions of the four synthesized alloys are (at. %) Ti45Zr45Nb5Ta5, Ti40Zr10Nb30Ta10Fe10, Ti25Zr25Hf25Nb12.5Ta12.5, and Ti20Zr20Ta20Hf20Nb20. They were selected because of their spread from being weakly anisotropic to highly anisotropic and insufficient knowledge of their elastic moduli. The alloys were prepared by arc melting in a water-cooled copper hearth under Ar atmosphere from Ti, Nb, Ta, Fe, Zr, and Hf elements with purity >99.9%. Each sample was 50 g in weight, and the melting process was repeated at least five times to ensure composition homogeneity. The samples were ground and polished using SiC abrasive papers. The phase constituents and corresponding lattice parameters were identified by X-ray diffraction with Co K α radiation (D8 Discover, Bruker, Germany). The Young's modulus was measured by using a sing-around ultrasonic velocity measuring instrument (UVM-2, Ultrasonic Engineering Co. Ltd., Japan), in which the longitudinal sound speed was measured for calculating the modulus. The mean value and standard deviation of five independent measurements were considered as the Young's modulus result. The hardness was measured using a micro Vickers hardness

testing machine (HM-200, Mitutoyo, Japan), and at least 15 independent measurements were conducted for each sample. The mean value and standard deviation were considered as the hardness result.

3. Texture modeling

To model the effect of crystallographic texture on the anisotropic elastic properties of poly-crystalline aggregates, relevant components of texture need to be defined. Generally, the nature of texture formed in a sample depends on the material and its preparation route (mechanical and thermal treatment). The present theoretical description is for single-phase RHEAs in the bcc structure. We focus, on the one hand, on fiber textures that typically develop in rolled bcc metals and alloys, and, on the other hand, on distinct textures that can develop by rapid directional solidification as observed in, for instance, β -Ti alloys manufactured by SLM. Both rolling and SLM are relevant in making Ti-based biomedical implant materials [43–48]. In the following, we first address the modeling of ODFs and define the sample coordinate systems. Second we introduce the considered texture components in detail.

The ODFs assumed a radially symmetric de la Vallée Poussin kernel with half-width κ . The half-width (full width at half-maximum) of the ODF kernel describes the spread of a single texture orientation and is related to texture sharpness. Texture sharpness is commonly quantified by the texture index t defined as [29],

$$t = \int_{SO(3)} f(g)^2 dg. \quad (14)$$

The effect of texture sharpness on the anisotropic elastic properties is examined as part of this work. The effective tensor averages (Section 2.2) were determined using an expansion of $f(g)$ into generalized spherical harmonics. All texture analysis was carried out with MTEX 5.4 [35,36].

The macroscopic sample shape was assumed to be orthotropic, which suggests use of a specific coordinate system. In the case of a rolled sample, we use a coordinate system whose x_1^S , x_2^S , and x_3^S axes coincide with the rolling direction (RD), transverse direction (TD), and normal direction (ND), respectively, see Fig. 1a1). In the case of a sample manufactured by SLM, we use a coordinate system whose x_1^S , x_2^S , and x_3^S axes coincide with the X scanning direction (XD), Y scanning direction (YD), and building direction (BD), respectively, see Fig. 1b1) or (c1). Direction dependent properties of samples are plotted as a function of spherical angles θ and ϕ , where θ measures the polar angle from the x_3^S direction and ϕ the azimuthal angle counterclockwise from the x_1^S direction in the x_1^S - x_2^S plane; see Figs. 1a1, b1, c1).

Rolling textures in bcc alloys were mostly studied for low-alloyed bcc refractory metals and Fe, high-alloyed steels, and β -Ti alloys. Cold rolling textures in these bcc materials are largely the same and not markedly altered by solute additions, e.g., Refs. [49–51,45] and references therein. Usually, α fiber-type and/or γ fiber-type textures tend to develop under rolling, with some variation in relative prominence of relevant texture orientations due to material or processing variation. We expect that the nature of cold-rolling texture in the current bcc RHEAs is not appreciably different from that in conventional bcc alloys, and thus mainly consider α -fiber and γ -fiber texture components. Recent investigations for a RHEA indicate that this expectation is justified [52,53].

We modeled the ODFs for two rolling textures referred to as RT_α and RT_γ with ODF portions as follows,

$$\begin{aligned} RT_\alpha &: 80\% \alpha - \text{fiber} + 10\% \gamma - \text{fiber} + 10\% \text{UNI}, \\ RT_\gamma &: 10\% \alpha - \text{fiber} + 80\% \gamma - \text{fiber} + 10\% \text{UNI}. \end{aligned}$$

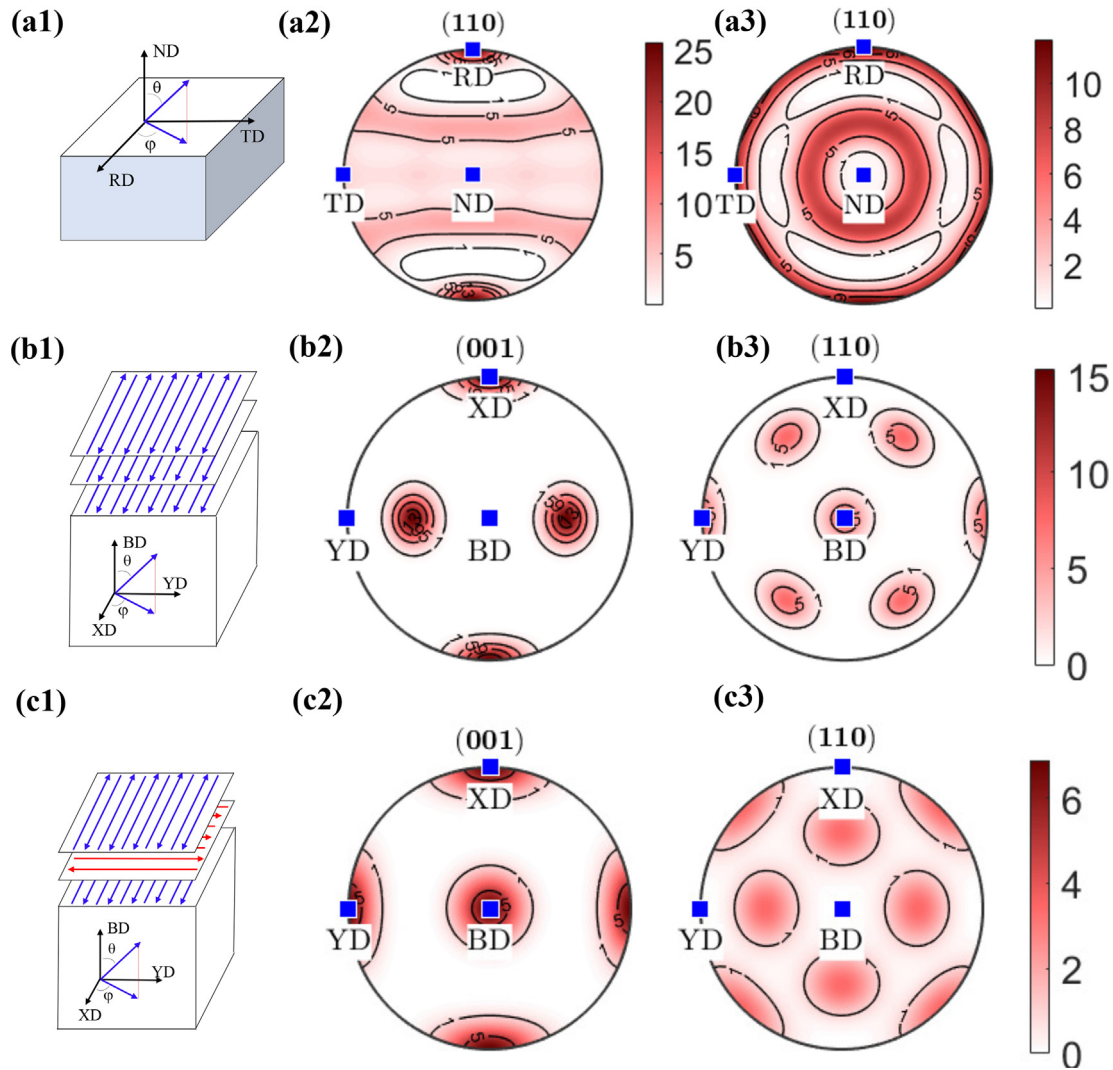


Fig. 1. (a1) Definition of the sample coordinate system for a rolled orthotropic sample. Panels (a2–a3) show simulated $\{110\}$ pole figures of rolling texture RT_x and RT_γ , respectively, with half-width $\kappa = 10^\circ$. (b1) Definition of the sample coordinate system for an orthotropic SLM-fabricated sample, and illustration of bidirectional scanning parallel to XD. Panels (b2) and (b3) show the $\{001\}$ and $\{110\}$ pole figures, respectively, for SLM_c texture. A half-width $\kappa = 10^\circ$ was used. Panels (c1–c3) are analogous to panels (b1–b3) but illustrate bidirectional scanning along XD and YD on alternating layers, and pole figures for SLM_c texture use a half-width of $\kappa = 15^\circ$. All pole figure plots are presented in equal area projection and show the upper hemisphere. Contours indicate multiples of uniform distribution.

The individual texture components, i.e., fibers and orientations, are defined in Table 1, while UNI denotes a uniform texture component. All orientations belonging to a fiber and all components belonging to a texture were assumed to have the same half-width. Rolling texture RT_x is characterized by a dominant (partial) α -fiber, and weak γ -fiber and uniform components, while in RT_γ the γ -fiber is the most pronounced. These texture features are

Table 1

Simulated texture components (fibers, orientations) in bcc alloys commonly described by the symbol $\{hkl\}[uvw]$ (also frequently $\{hkl\}\langle uvw \rangle$). The crystallographic plane (hkl) lies parallel to the RD-TD surface (rolling plane, sheet surface) or XD-YD surface (scanning plane). The crystallographic $[uvw]$ direction lies parallel to RD or XD.

component	fiber axis and/or relevant orientations
α -fiber	$[1\bar{1}0] \parallel \text{RD}$, from $(001)[1\bar{1}0]$ to $(111)[1\bar{1}0]$
γ -fiber	$[111] \parallel \text{ND}$, from $(111)[1\bar{1}0]$ to $(111)[\bar{1}12]$
cube	$(001)[100]$
Goss	$(011)[100]$

clearly reflected in the simulated $\{110\}$ pole figures shown in Figs. 1a2) and (a3). A half-width of $\kappa = 10^\circ$ was used to produce both pole figure plots. The contours in the pole figure plots indicate multiples of uniform distribution: in cases where there is texture the weaker areas have a value less than one and the stronger areas have a value greater than one.

Recent experimental work for Ni–Mo and β -Ti alloys suggested that crystallographic texture in samples manufactured by SLM can be tailored by control of process conditions [46–48]. Specifically, the preferential growth orientation of columnar cells dependent on scanning strategy reported in the work of Ishimoto et al. on bcc Ti–15Mo–5Zr–3Al alloy [46] motivates below SLM textures. In this paper, we presume that texture design by control of SLM process conditions can also be achieved in the alloys studied in the present work (it is not implied, however, that a certain scanning strategy applied to different alloys results in the same preferential cell orientation; Figs. 1b1) and (c1) and accompanying text serve as illustration).

We modeled the ODFs for two different SLM textures referred to as SLM_c and SLM_γ with ODF portions as follows,

SLM_C : 100%cube,
SLM_C : 100%Goss.

SLM_C models a texture with preferential orientation of {011} cells along the BD, which in Ref. [46] was accomplished by bidirectional scanning parallel to XD [Fig. 1b1)]. On the other hand, bidirectional scanning along XD and YD on alternating layers [Fig. 1c1)] resulted in a preferential orientation of {001} cells along the BD (Ref. [46]), which we describe by SLM_C. In Figs. 1(b2-b3) and (c2-c3) we show the simulated {001} and {110} pole figures for both SLM textures. Two different half-widths, $\kappa = 10^\circ$ and 15° , were used to visualize the effect of texture sharpness on the pole figure plots. It should be noted that pole figures reported in Ref. [46] were measured in the YD-BD plane, while the present pole figures are for the XD-YD plane.

4. Results

4.1. Experimental results

Fig. 2 shows the X-ray diffraction spectra of the synthesized Ti45Zr45Nb5Ta5, Ti25Zr25Hf25Nb12.5Ta12.5, Ti20Zr20Ta20Hf20Nb20, and Ti40Zr10Nb30Ta10Fe10 RHEAs. The bcc phase is observed in all four alloys. Ti40Zr10Nb30Ta10Fe10 also exhibits an intermetallic phase in minor volume fraction as judged by diffraction peak intensity. The derived lattice parameters of the

bcc phases (a_{exp}) are listed in Table 2 along with the measured Young's moduli ($E_{\text{iso,exp}}^S$) and Vickers hardnesses ($H_{V,\text{exp}}$). $E_{\text{iso,exp}}^S$ and $H_{V,\text{exp}}$ are the lowest for Ti45Zr45Nb5Ta5 and increase with the fraction of non-Group 4 elements in the sequence Ti25Zr25Hf25Nb12.5Ta12.5, Ti20Zr20Ta20Hf20Nb20, and Ti40Zr10Nb30Ta10Fe10. The present Vickers hardness of Ti20Zr20Ta20Hf20Nb20 is comparable to a previous measurement with a Berkovich indenter (3.14 ± 0.12 GPa; pile up corrected value) [13]. These a_{exp} and $E_{\text{iso,exp}}^S$ values along with literature data are used for validation of the theoretical results in the following subsections.

4.2. Theoretical elastic properties of single-crystal refractory high-entropy alloys

The intrinsic elastic anisotropy in single crystals of cubic symmetry renders them interesting for single-crystal implant materials, as the directional dependence of Young's modulus can be exploited to match the properties of bone. Thus, it is necessary to investigate the direction dependence of Young's modulus and determine directions of minimum Young's modulus. By the latter we understand the minimum across all possible directions of uniaxial load, $\min_{\mathbf{n}} E(\mathbf{n})$. Similarly, the maximum Young's modulus is $\max_{\mathbf{n}} E(\mathbf{n})$. To this end, we start by presenting the single-crystal

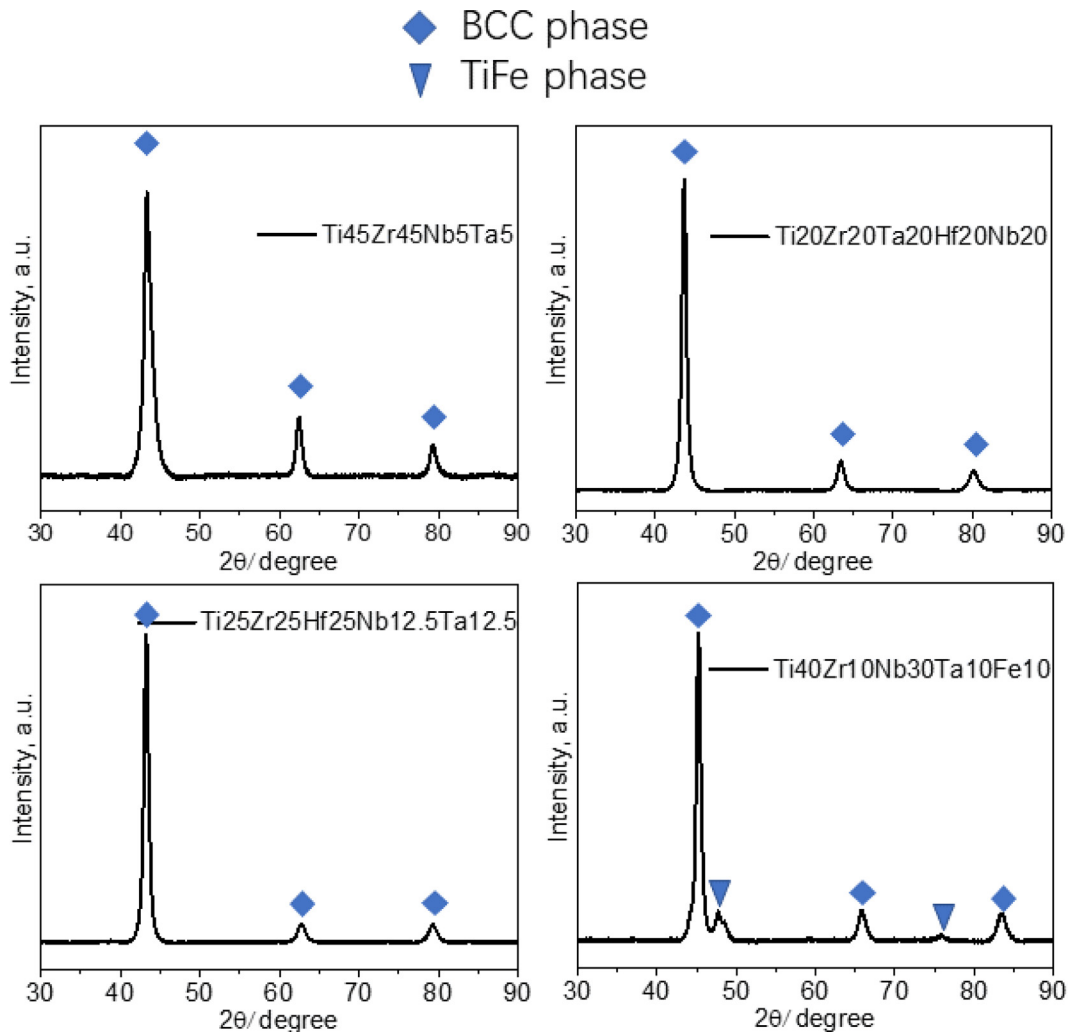


Fig. 2. X-ray diffraction patterns of Ti45Zr45Nb5Ta5, Ti25Zr25Hf25Nb12.5Ta12.5, Ti20Zr20Ta20Hf20Nb20, and Ti40Zr10Nb30Ta10Fe10 HEAs.

Table 2

Room temperature lattice parameter of the bcc phase (in Å), Young's modulus (in GPa), and Vickers hardness (in GPa) for the four experimentally investigated RHEAs.

RHEA	a_{exp}	$E_{\text{iso,exp}}^S$	$H_{V,\text{exp}}$
Ti45Zr45Nb5Ta5	3.435	79±2	2.55±0.05
Ti25Zr25Hf25Nb12.5Ta12.5	3.435	81±2	3.48±0.09
Ti20Zr20Ta20Hf20Nb20	3.405	94±2	3.67±0.15
Ti40Zr10Nb30Ta10Fe10	3.292	107±2	5.66±0.25

elastic constants C_{11} , C_{12} , and C_{44} , and then proceed to the derived elastic properties including Young's modulus.

Table 3 lists the chemical compositions of the 21 presently considered biocompatible RHEAs. These alloys were recently synthesized [17,11,13,14,12,10,9] and in most cases exhibited the bcc phase (the three alloys from Ref. [11] were not bulk crystals but consolidated powders). As is obvious, Ti is contained in all 21 alloys, of which 19 are non-equimolar alloys. For the sake of convenience, Table 3 and all following tables list the RHEAs in increasing order of their average valence electron count (VEC). Presenting the elastic properties of these alloys versus VEC turned out to be an insightful way to visualize alloying trends.

Table 3 also presents the calculated equilibrium lattice parameters and three independent elastic constants of all the considered alloys. Good agreement (maximum absolute error of 1.3%) is found between the calculated lattice parameters and the experimental room-temperature data from current experiments (Table 2) and previous experiments (Table 3). The bcc phase of all considered RHEAs is predicted to be elastically stable at zero temperature and pressure judged from the Born criteria, $C_{44} > 0$, $C_{11} - |C_{12}| > 0$, and $C_{11} + 2C_{12} > 0$ [25]. The elastic stability is consistent with the experimentally observed bcc phase at ambient conditions.

For the analysis and discussion to follow, we also present in Table 3 the tetragonal shear modulus C' and the universal anisotropy index A_u . Fig. 4(a) shows that there is a strong reciprocal correlation between A_u and VEC. As is evident, A_u starkly decreases from ~ 4.2 to slightly larger than zero in a relatively narrow range of VEC values (4.1–4.8). As a larger elastic anisotropy gives a larger deviation of A_u from zero, single-crystal Ti45Zr45Nb5Ta5 turns out

to be the most anisotropic material and Ti40Zr10Nb30Ta10Fe10 the most isotropic one.

The variation of Young's modulus with loading direction allows for two possible directions of minimum value in cubic single crystals, i.e., $\langle 001 \rangle$ or $\langle 111 \rangle$ [we omit the intrinsically isotropic case given by Eq. (1)]. This is a consequence of the N^4 term in Eq. (3), which is zero for the directions of the cube axes $\langle 001 \rangle$ and has its maximum value of $1/3$ in the $\langle 111 \rangle$ directions. The sign of $2S_{11} - 2S_{12} - S_{44}$ determines which of the two sets of directions has the minimum Young's modulus. The directions of maximum value are, by necessity, the respective other set of directions. For all the alloys investigated presently, we observe that $\langle 001 \rangle$ are the directions of the softest Young's modulus, see Table 5 for detailed numerical values. Therein we also compare to Young's modulus in the $\langle 011 \rangle$ directions (corresponding $N^4 = 0.25$) and the $\langle 111 \rangle$ directions.

The nearly reciprocal relation between elastic anisotropy and VEC explains why the relative spread between $E(\langle 001 \rangle)$ and $E(\langle 111 \rangle)$ tends to diminish with VEC (Table 5). The full dependence of $E(n)$ on loading direction for the alloy with the smallest A_u (Ti40Zr10Nb30Ta10Fe10) and the alloy with the largest A_u (Ti45Zr45Nb5Ta5) are contrasted by surface plots in Fig. 3(a). A clear correlation between the magnitude of the universal anisotropy index and the shape of the Young's modulus surface is apparent.

Turning to the torsion modulus $T(n)$, its variation with torque axis [Eq. (5)] depends on the same N^4 angular term as Young's modulus. However, there is a sign difference of the $2S_{11} - 2S_{12} - S_{44}$ term, which results in a different direction dependence. Table 5 presents numerical values for T when the torque axis equals $\langle 001 \rangle$, $\langle 011 \rangle$, or $\langle 111 \rangle$. T has its maximum value in the directions of the cube axes $\langle 001 \rangle$ and its minimum value in the $\langle 111 \rangle$ directions, reciprocal to the behavior of $E(n)$. The torsion anisotropy, i.e., difference between the maximum and minimum moduli, tends to decrease with VEC as it is linked to the behavior of elastic anisotropy. The effect of elastic anisotropy is further reflected in the shape of the representation surface of $T(n)$ as a function of torque axis shown in Fig. 3(b), which is highly anisotropic for Ti45Zr45Nb5Ta5 but nearly isotropic for Ti40Zr10Nb30Ta10Fe10.

Table 3

Calculated material property values of bcc RHEAs from present theory. The reference to each alloy indicates previous synthesis and structure determination. The alloys are listed in increasing order of VEC and all compositions are in atomic percentage. The equilibrium lattice parameters from present theory a along with experimental values a_{exp} from available literature (all in Å), the theoretical elastic constants and derived tetragonal shear moduli (rounded to whole GPa), and universal anisotropy indexes are given.

RHEA	VEC	a	a_{exp}	C_{11}	C_{12}	C_{44}	C'	A_u
Ti45Zr45Nb5Ta5 [14]	4.10	3.412	-	112	87	65	12	4.227
Ti26.3Zr26.3Hf26.3Nb10.55Ta10.55 [14]	4.21	3.415	-	145	100	73	23	1.814
Ti25Zr25Hf25Nb12.5Ta12.5 [14]	4.25	3.410	-	151	101	72	25	1.493
Ti37.5Zr25Ta12.5Hf12.5Nb12.5 [13]	4.25	3.383	3.405 [13]	146	99	68	23	1.541
Ti23.8Zr23.8Hf23.8Nb14.3Ta14.3 [14]	4.29	3.405	-	156	102	71	27	1.255
Ti35Zr35Nb25Ta5 [14]	4.30	3.384	-	142	91	58	26	0.847
Ti21.7Zr21.7Hf21.7Nb17.45Ta17.45 [14]	4.35	3.397	-	164	104	70	30	0.924
Ti31.67Zr31.67Nb31.66Ta5 [14]	4.37	3.376	-	152	92	56	30	0.480
Ti20Zr20Ta20Hf20Nb20 [13]	4.40	3.390	3.429 [13]	175	109	69	33	0.709
Ti25Nb25Ta25Zr25 [9]	4.50	3.364	3.32 [9]	174	101	60	37	0.311
Ti30.5Zr30.5Nb13Ta13Mo13 [12]	4.52	3.345	-	175	97	57	39	0.175
Ti34Zr20Nb20Ta20Mo6 [12]	4.52	3.335	-	180	102	60	39	0.230
Ti21.67Zr21.67Nb21.66Ta35 [14]	4.57	3.359	-	187	107	63	40	0.258
Ti23.8Zr23.8Hf23.8Cr4.8Mo23.8 [17]	4.57	3.334	3.37 [17]	192	106	61	43	0.145
Ti30Zr20Nb20Ta20Mo10 [12]	4.60	3.328	-	192	104	58	44	0.093
Ti24.2Zr24.2Hf24.2Co1.6Cr1.6Mo24.2 [17]	4.60	3.339	3.36 [17]	191	105	62	43	0.167
Ti39.4Nb15.15Ta15.15Zr15.15Mo15.15 [10]	4.61	3.300	3.30 [10]	195	104	58	45	0.071
Ti40Zr20Nb20Ta10Fe10 [11]	4.70	3.291	-	173	93	58	49	0.176
Ti15Zr15Nb35Ta35 [14]	4.70	3.345	-	210	112	60	49	0.047
Ti40Zr15Nb25Ta10Fe10 [11]	4.75	3.278	-	183	95	58	44	0.093
Ti40Zr10Nb30Ta10Fe10 [11]	4.80	3.265	-	193	98	57	48	0.040

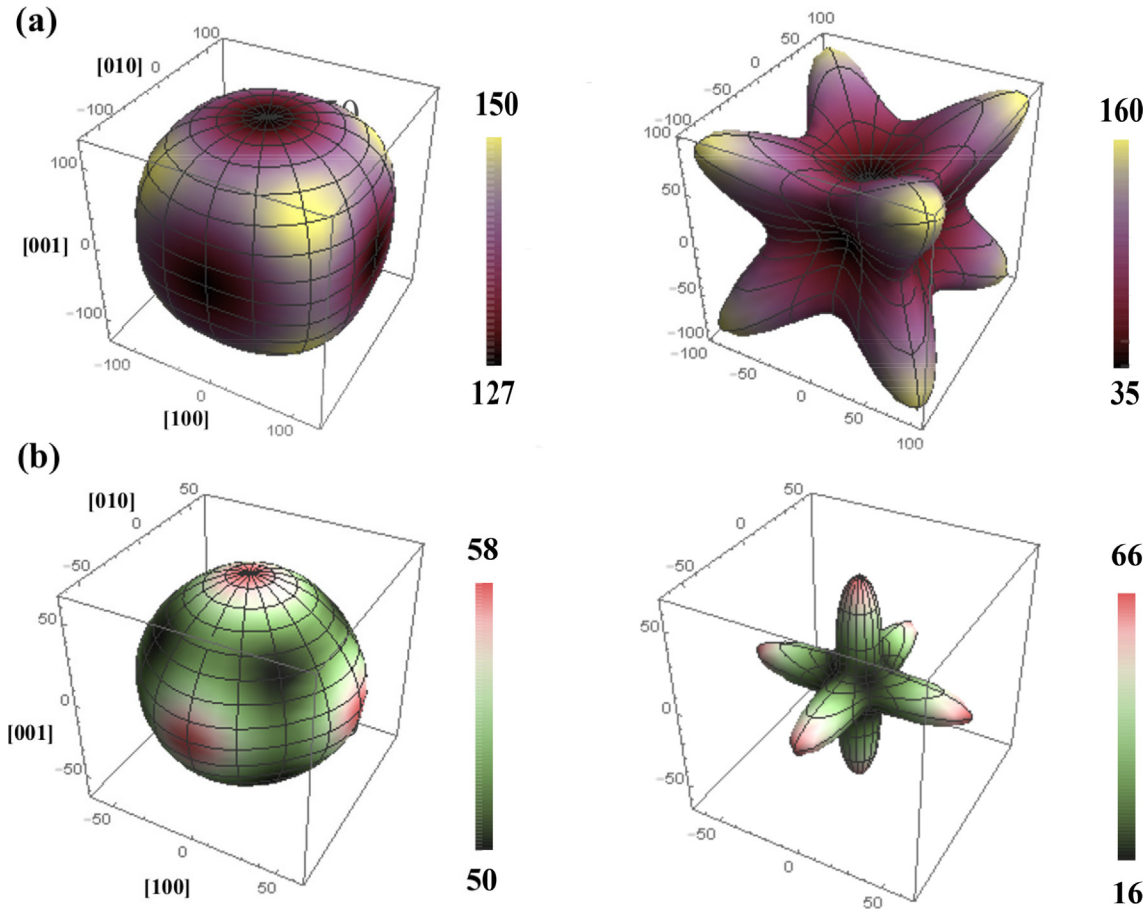


Fig. 3. (a) Representation of direction dependence of Young's modulus $E(\mathbf{n})$ in single-crystal Ti40Zr10Nb30Ta10Fe10 (left) and Ti45Zr45Nb5Ta5 (right). (b) Representation of direction dependence of the torsion modulus $T(\mathbf{n})$ in single-crystal Ti40Zr10Nb30Ta10Fe10 (left) and Ti45Zr45Nb5Ta5 (right). The magnitudes of E and T (in units of GPa) along loading direction \mathbf{n} is proportional to the radius from the point of origin. The Cartesian axes correspond to the projections onto the [100], [010], and [001] crystallographic axes. Note the different color bars.

It is insightful for the purpose of alloy design to understand which parameters predominantly determine the alloying effect on the moduli for the present RHEAs. To this end, we first analyze whether any elastic constant, or combination thereof, dominates the alloying effect on $E(\langle 001 \rangle)$ and $T(\langle 111 \rangle)$. For \mathbf{n} in these directions, we write Eqs. (3) and (5) as, respectively,

$$E(\langle 001 \rangle) = \frac{3}{(C_{11} + 2C_{12})^{-1} + C'^{-1}}, \quad (15a)$$

$$T(\langle 111 \rangle) = \frac{3}{C_{44}^{-1} + 2C'^{-1}}. \quad (15b)$$

The numerical values in Table 3 suggest that C' exerts the dominant alloying effect. Indeed, strong positive and nearly linear correlations between $E(\langle 001 \rangle)$ and C' and between $T(\langle 111 \rangle)$ and C' are evident in Fig. 4(b).

The tetragonal shear elastic constant C' of the transition elements is well known to vary regularly across any of the three transition metal element series [54,55]. This canonical behavior is rooted in the electronic structure of transition metals and mostly determined by the d -band filling. The canonical trend was recently shown to be preserved in binary transition metal alloys [56]. While the d -band filling is readily accessible to first-principles simulations, for practical purposes the VEC can be drawn upon instead. Note that increases of d -band filling go in parallel with increases of VEC.

Fig. 4(c) shows that the $E(\langle 001 \rangle)$ and $T(\langle 111 \rangle)$ increase with VEC of RHEAs. The correlations are approximately linear despite some apparent scatter. A reason for why the correlations between either modulus with C' is better than with VEC is that C' takes into account electronic structure differences between the transition metal series (resulting in elastic constants differences between 3d, 4d, and 5d series for the same band filling parameter), but the VEC does not. Nonetheless, the quality of the correlation suggests that the VEC may serve as an easily accessible and fairly accurate parameter to tailor the single-crystal properties of the present and related RHEAs.

4.3. Theoretical elastic properties of poly-crystalline, isotropic aggregates of refractory high-entropy alloy

In a poly-crystalline, statistically isotropic material all possible orientations of crystallites occur with equal frequency. Such a poly-crystalline material behaves elastically isotropically on the whole, even though a single crystallite is anisotropic. The results for poly-crystalline aggregates presented in this section mainly serve two purposes: (i) they allow to compare our theoretical results with experimental elastic moduli obtained for quasi-isotropic poly-crystals, and (ii) they are used as reference level for discussing the effect of texture (Section 4.4).

We first present our theoretical results mainly focusing on trends. The totality of calculated data (bulk modulus B_{iso}^S , torsion modulus T_{iso}^S , and Young's modulus E_{iso}^S) is shown in Table 5. Note

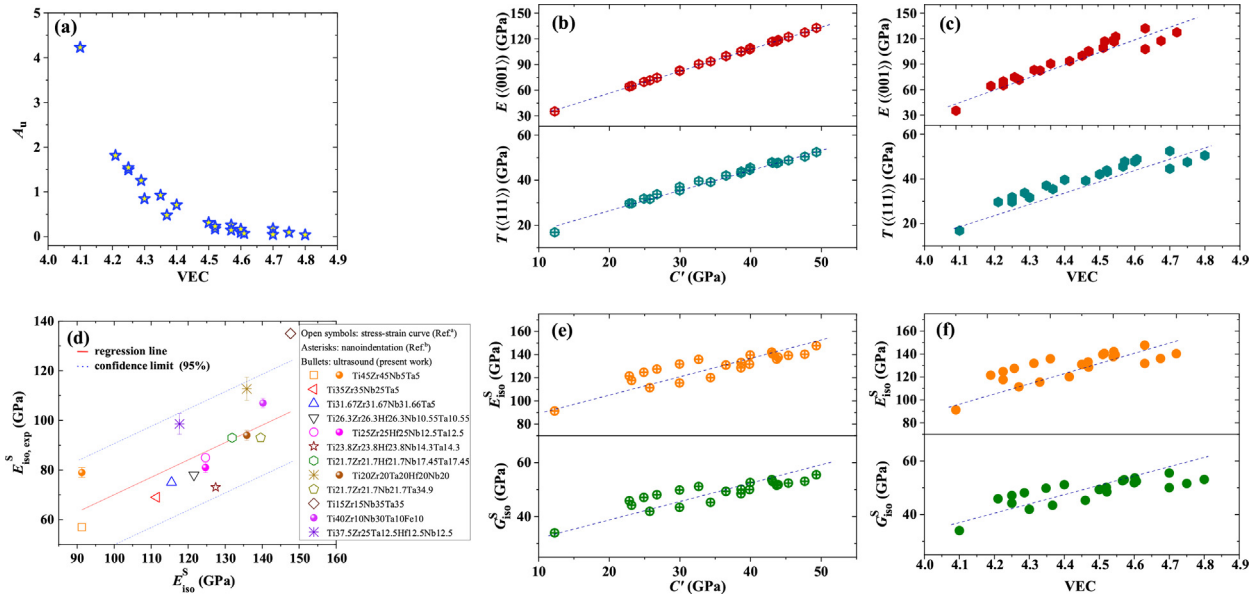


Fig. 4. Trends and correlations in elastic properties of single-crystal RHEAs and their isotropic poly-crystalline aggregates. (a) Elastic anisotropic index A_u as a function of VEC. (b) Single-crystal Young's modulus $E_{(001)}$ and torsion modulus $T_{((111))}$ plotted versus the shear elastic constant C' . Panel (c) is analogous to panel (b) but both moduli are plotted versus VEC. (d) Correlation between calculated and experimental Young's moduli (Ref.^a: Yuan *et al.* [14]; Ref.^b: Motallebzadeh *et al.* [13]). (e) Young's modulus E_{iso}^S and torsion modulus T_{iso}^S for poly-crystalline, isotropic aggregates plotted versus the single-crystal shear constant C' . Panel (f) is analogous to panel (e) but both moduli are plotted versus VEC. Lines guide the eye.

that $G_{iso}^S = T_{iso}^S$. The ratio E_{iso}^S/G_{iso}^S approximates 2.65 for all the studied alloys, which is close to the empirical ratio of $\approx 8/3$ known from poly-crystalline metallic elements [57].

Fig. 4(e) shows systematic positive correlations between the poly-crystal Young's and shear moduli and the single-crystal shear constant C' . Fig. 4(f) shows that both moduli are also positively correlated with the VEC. G_{iso}^S and E_{iso}^S correlate less strongly with either C' or VEC than the single-crystal counterparts from Figs. 4(b) and (c). The reason is that the alloying effect is not dominated by C' in a general loading direction or torque axis.

Second, we statistically analyze the difference between the Young's modulus from present theory and available experimental data by means of a simple linear regression [58]. The regression with regression line $E_{iso,exp}^S = \chi E_{iso}^S$ was carried out by means of a least-squares fit. Here, we selected the experimental modulus $E_{iso,exp}^S$ as the dependent variable and the theoretical modulus E_{iso}^S as the independent one. Comparing χ to 1 quantifies any systematic deviation between experiment and theory, whereas the standard deviation of the regression error describes the residual error bar [58]. Experimental error bars are not considered in the model.

The available experimental results comprise data from present experiments (four alloys) and data obtained in previous measurements (ten alloys, data from Refs. [13,14]). Different methods were employed to obtain the experimental Young's moduli: tensile stress-strain line [14], nano-indentation load-displacement curve [13], or ultrasound (present experiments).

In Fig. 4(d) we present the linear regression between experimental and theoretical Young's moduli. The obtained systematic deviation $1 - \chi$ is 0.3 and the absolute residual error bar assuming a 95% confidence interval is 20 GPa, which corresponds to a 20–30% relative residual error with respect to the experimental values. The residual error bar is indicated by dashed lines in Fig. 4(d). The relative error for Young's modulus is of comparable scale to the DFT errors determined previously for elastic constants and bulk modulus [58]. Although the general trend is predicted correctly,

there is a systematic deviation from a perfect correlation $E_{iso,exp}^S = E_{iso}^S$. Note that no experimental or theoretical data point was considered to be an outlier and removed from the regression analysis.

Several reasons could cause this systematic deviation. On the theoretical side, besides the Hill approximation, the considered alloys may contain one or several elements, the elastic properties of which DFT or the present method does not reproduce accurately [58,59]. These include zirconium and niobium, which can disproportionately distort the agreement between experiment and theory. Furthermore, our theoretical values are valid at zero temperature, whereas the experimental coefficients were obtained at ambient temperature. Raising the temperature to ambient conditions is expected to reduce the magnitude of elastic parameters. In lack of experimental data for the present RHEAs, we consider the experimental single-crystal elastic constants of non-magnetic bcc refractory elements, which typically reduce by 2–7% in 4.2 to 300 K [60,61]. A temperature-corrected Young's modulus assuming the same percentage value would thus generally improve the agreement between present theory and the available experiments.

On the experimental side, we note that all the measurements were carried out on as cast samples, which in some cases exhibited a dendritic morphology. A homogeneous microstructure could be accomplished via suitable thermal processing and might alter the elastic properties somewhat, depending on the degree of elemental segregation in the as cast state. Moreover, the Young's moduli of three alloys with nominally similar composition, Ti45Zr45Nb5Ta5, Ti25Zr25Hf25Nb12.5Ta12.5, and Ti20Zr20Ta20Hf20Nb20, were determined by two dissimilar techniques. In the first and the last alloy case, there is a noticeable spread of the Young's modulus' value (10–20 GPa) across the experimental methods employed. These differences may reflect methodological challenges of measuring Young's modulus, such as evaluation of contact area and pile-up correction in nanoindentation, as well as differences in sample condition owing to preparation method including chemical homogeneity.

4.4. Theoretical elastic properties of poly-crystalline, textured aggregates of refractory high-entropy alloys

The effect of non-random crystallographic texture on the macroscopic elastic properties were theoretically investigated for all 21 considered RHEAs. Results for three of them are analyzed in detail in the following. The selected alloys are Ti45Zr45Nb5Ta5, Ti37.5Zr25Ta12.5Hf12.5Nb12.5, and Ti40Zr10Nb30Ta10Fe10 and represent, respectively, a highly anisotropic material ($A_u=4.227$), a moderately anisotropic material (1.541), and a weakly anisotropic material (0.040). We recall that the values of A_u for the other 18 alloys lie in between the bound of 0.040 and 4.227, from which conclusions on trends may be drawn. In Section 5 we summarize and discuss the minimum Young's modulus for the totality of 21 examined alloys.

Texture introduces orientation dependences of Young's modulus and torsion modulus in poly-crystalline materials, which in the present study depends on the specific texture and texture sharpness. For the considered rolling textures and SLM textures, respectively, the symmetry of the effective compliance tensor is orthorhombic and cubic. The minimum Young's modulus across all possible directions of uniaxial load, $\langle E^S \rangle(\theta_{\min}, \phi_{\min}) \equiv \min_{\theta, \phi} \langle E^S \rangle(\theta, \phi)$, is of primary interest in the following. Table 4 shows that both RT_α and RT_γ textures in Ti45Zr45Nb5Ta5 can moderately reduce Young's modulus below the isotropic value of 91 GPa. For either rolling texture, a sharper texture, as quantified by a larger texture index t , has the effect of reducing the minimum Young's modulus. This is due to a decrease in spread of texture orientations (smaller half-width κ). Simultaneously, the anisotropy of Young's modulus, if measured by the difference between maximum and minimum values (Table 4), increases with texture sharpening. Both trends are more pronounced for RT_γ than RT_α . This can be understood from the higher texture index of RT_γ for the same κ value. Furthermore, changes in $\langle E^S \rangle(\theta, \phi)$ with κ depend on the loading direction under consideration. The direction of minimum Young's modulus does not lie parallel to RD, TD, or ND for either RT_α or RT_γ texture. The direction of the maximum Young's modulus for RT_γ (Table 4) is along ND, since the dominant γ -fiber component preferably aligns one of the $\langle 111 \rangle$ single-crystal directions parallel to ND. The directions of the minimum Young's modulus for RT_α and RT_γ cases agree incidentally, as both textures contain α -fiber and γ -fiber components.

Table 4

Elastic anisotropy of Young's modulus $\langle E^S \rangle$ and $\overline{\langle T^S \rangle}(\theta_{\min}, \phi_{\min})$ in poly-crystalline Ti45Zr45Nb5Ta5 possessing rolling-type texture or SLM-type texture for various texture sharpnesses. The texture sharpness is characterized by the texture index t determined for three different half-widths of the ODF kernel κ describing the spread of a single texture orientation. The value of Young's modulus in special sample directions [(RD, TD, ND) or (XD, YD, BD)] is shown along with the minimum and maximum values across all directions with corresponding angles θ and ϕ . Among equivalent directions of minimum and maximum Young's moduli, only those with the lowest θ , then lowest ϕ are given. The moduli are in units of GPa and the angles in degree.

Rolling texture	κ	t	Anisotropy of Young's modulus $\langle E^S \rangle$									
			RD	TD	ND	min	θ_{\min}	ϕ_{\min}	max	θ_{\max}	ϕ_{\max}	$\overline{\langle T^S \rangle}(\theta_{\min}, \phi_{\min})$
RT_α	5°	11	106	98	100	84	48	27	106	90	0	32
	10°	3	104	97	99	85	48	27	104	90	0	36
	15°	2	101	95	97	87	48	27	101	90	0	36
RT_γ	5°	20	106	105	136	76	46	21	136	0	0	38
	10°	6	104	103	127	78	46	23	127	0	0	38
	15°	3	101	100	116	82	47	25	117	0	0	37
SLM texture	κ	t	XD	YD	BD	min	θ_{\min}	ϕ_{\min}	max	θ_{\max}	ϕ_{\max}	$\overline{\langle T^S \rangle}(\theta_{\min}, \phi_{\min})$
SLM _C	5°	182	38	38	38	38	0	0	152	55	45	62
	10°	23	46	46	46	46	0	0	138	55	45	55
	15°	7	56	56	56	56	0	0	124	55	45	48
SLM _G	5°	182	38	87	87	38	45	90	152	35	0	62
	10°	23	46	92	92	46	45	90	138	35	0	55
	15°	7	56	95	95	56	45	90	124	35	0	48

Figs. 5(a) and (b) illustrate how $\langle E^S \rangle(\theta, \phi)$ varies with loading direction for textured aggregates of Ti45Zr45Nb5Ta5 possessing RT_α texture and RT_γ texture, respectively. The half-width of ODF kernel is 10° in both plots. As is evident, $\langle E^S \rangle(\theta, \phi)$ for RT_γ shows approximate rotational symmetry around ND due to the parallel-aligned γ -fiber axis (the weak α -fiber component prevents perfect rotational symmetry). Approximate rotational symmetry also implies that low values of $\langle E^S \rangle(\theta, \phi)$ are found in a concentric region around ND at a polar angle of $\approx 48^\circ$.

The presence of SLM-type texture in Ti45Zr45Nb5Ta5 can substantially lower Young's modulus below the isotropic value, see Table 4. Simultaneously, a large anisotropy of Young's modulus is introduced. Sharper texture leads to lower minimum Young's modulus and higher maximum Young's modulus, similar to the effect of texture sharpening in the case of the rolling textures. For the same value of the half-width, the amplitude of deviation from the E_{iso}^S is obviously higher for the SLM-type textures than for the fiber textures. These observations directly result from the presence of cube or Goss texture components and the absence of fibers, which preserve much of the single-crystal elastic character in the SLM textured specimens. This is also reflected in a higher texture index t , signifying that many crystallites possess similar orientation. The smaller the spread of cube or Goss texture orientations, the more closely the single-crystal elastic properties are retained. An obvious difference between SLM_C and SLM_G is that the minimum Young's modulus appears along the XD, YD, and BD sample directions for the former, but only along XD for the latter. This is a consequence of the fact that cube and Goss textures orient individual grains differently with respect to the sample coordinate system. In practice, one of the two textures and associated direction of minimum Young's modulus might, however, be preferred for different reasons, including machining the implant, or having the lowest Young's modulus pointing in a certain direction relative to the melt pool boundaries.

Figs. 5(c) and (d) illustrate the direction dependence of Young's modulus for poly-crystalline aggregates of Ti45Zr45Nb5Ta5 possessing SLM-type textures. Panel (c) is for SLM_C with $\kappa = 10^\circ$ and panel (d) for SLM_G with $\kappa = 15^\circ$. Similar to the pole figure plots in Figs. 1(b2-b3) and (c2-c3), two different half-widths of ODF kernel were employed to visualize the effect of texture sharpness on the anisotropy of Young's modulus. Clearly, a sharper texture

Table 5

Elastic properties (rounded to whole GPa) of bcc RHEAs from present theory. Shown are the single-crystal Young's moduli and torsion moduli in various high-symmetry directions and the elastic moduli of isotropic poly-crystalline aggregates. Note that $G_{\text{iso}}^S = T_{\text{iso}}^S$.

RHEA	$E(\langle hkl \rangle)$			$T(\langle hkl \rangle)$			B_{iso}^S	T_{iso}^S	E_{iso}^S
	$\langle 001 \rangle$	$\langle 011 \rangle$	$\langle 111 \rangle$	$\langle 001 \rangle$	$\langle 011 \rangle$	$\langle 111 \rangle$			
Ti45Zr45Nb5Ta5	35	85	160	65	21	17	95	34	91
Ti26.3Zr26.3Hf26.3Nb10.55Ta10.55	64	124	181	73	35	30	115	46	122
Ti25Zr25Hf25Nb12.5Ta12.5	70	129	180	72	37	32	117	47	125
Ti37.5Zr25Ta12.5Hf12.5Nb12.5	65	122	171	68	35	30	115	44	118
Ti23.8Zr23.8Hf23.8Nb14.3Ta14.3	75	133	179	71	39	34	120	48	127
Ti35Zr35Nb25Ta5	72	117	148	58	36	32	108	42	111
Ti21.7Zr21.7Hf21.7Nb17.45Ta17.45	83	138	177	70	42	37	124	50	132
Ti31.67Zr31.67Nb31.66Ta5	83	121	144	56	39	35	112	43	116
Ti20Zr20Ta20Hf20Nb20	90	143	177	69	44	40	131	51	136
Ti25Nb25Ta25Zr25	100	137	156	60	46	42	125	49	131
Ti30.5Zr30.5Nb13Ta13Mo13	105	134	147	57	46	43	123	49	129
Ti34Zr20Nb20Ta20Mo6	105	139	155	60	47	44	128	50	133
Ti21.67Zr21.67Nb21.66Ta35	109	146	164	63	49	46	134	53	140
Ti23.8Zr23.8Hf23.8Cr4.8Mo23.8	117	146	159	61	51	48	134	53	141
Ti30Zr20Nb20Ta20Mo10	119	142	152	58	50	48	133	52	138
Ti24.2Zr24.2Hf24.2Co1.6Cr1.6Mo24.2	117	148	162	62	51	48	134	54	142
Ti39.4Nb15.15Ta15.15Zr15.15Mo15.15	122	143	152	58	51	49	134	52	139
Ti40Zr20Nb20Ta10Fe10	108	137	151	58	47	45	120	50	132
Ti15Zr15Nb35Ta35	133	152	158	60	54	53	144	56	148
Ti40Zr15Nb25Ta10Fe10	117	140	150	58	50	48	124	52	136
Ti40Zr10Nb30Ta10Fe10	127	143	150	57	52	51	129	53	140

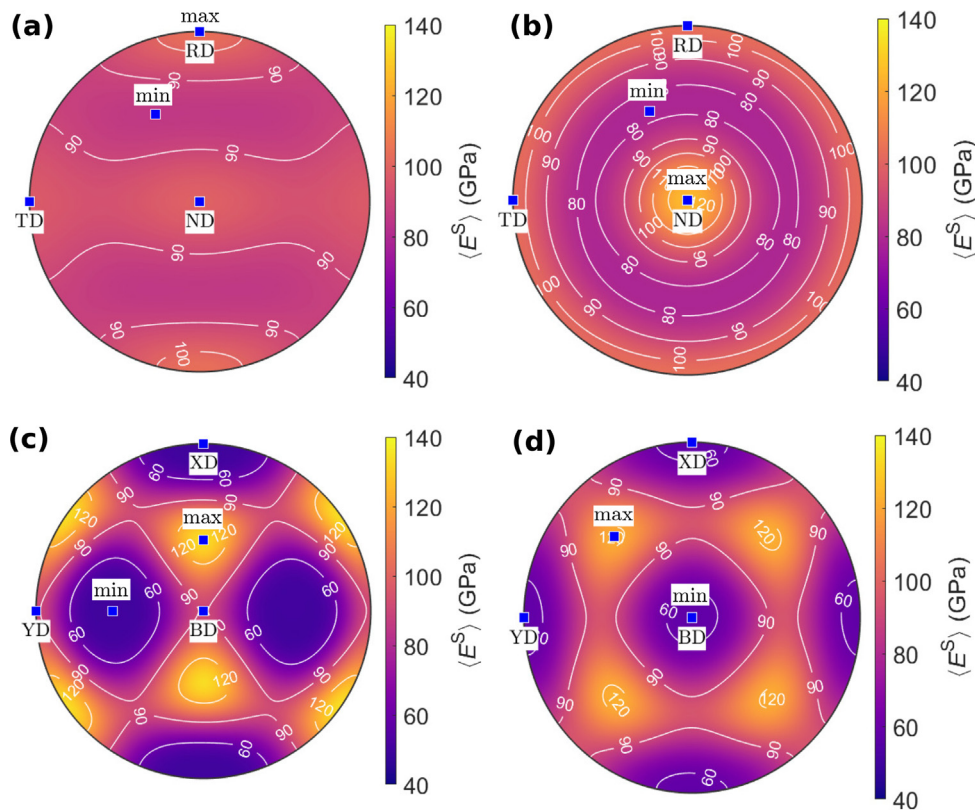


Fig. 5. Panel (a) is for RT_x texture and panel (b) for RT_γ texture ($\kappa = 10^\circ$). Panel (c) is for SLM_c texture ($\kappa = 10^\circ$) and panel (d) is for SLM_c texture ($\kappa = 15^\circ$). Among equivalent directions of minimum and maximum Young's moduli, only those with the lowest θ , then lowest ϕ are indicated. Identical color bars were chosen to easily compare the macroscopic elastic anisotropy.

increases the anisotropy of $\langle E^S \rangle(\theta, \phi)$, and the difference of cube and Goss orientations reflects in how $\langle E^S \rangle(\theta, \phi)$ varies with loading direction.

Turning to the torsion modulus in Ti45Zr45Nb5Ta5, we consider the case when the torque axis is placed parallel to the sample direction of minimum Young's modulus. The moduli are thus

denoted by $\overline{\langle T^S \rangle}(\theta_{\min}, \phi_{\min})$ and their values for the various textures are given in Table 4. The examined non-random crystallographic textures, except RT_x with $\kappa = 5^\circ$, increase $\overline{\langle T^S \rangle}(\theta_{\min}, \phi_{\min})$ relative to the isotropic value T_{iso}^S . With decreasing κ , $\overline{\langle T^S \rangle}(\theta_{\min}, \phi_{\min})$ may increase (SLM textures; converge to

$T(\langle 001 \rangle)$), decrease (RT_x) or remain practically constant (RT_y). Further, the torsion moduli for RT_x and RT_y are well below those of the SLM textures. This follows since the crystal directions of lowest Young's modulus in bcc crystals are simultaneously the directions with the largest torsion modulus.

The results for Ti37.5Zr25Ta12.5Hf12.5Nb12.5 and Ti40Zr10Nb30Ta10Fe10 are summarized in Table 6 and Table 7, respectively. We observe several qualitative similarities between these two RHEAs and Ti45Zr45Nb5Ta5 for both rolling and SLM type textures: (i) the relative anisotropy of $\langle E^S \rangle$ in directions parallel to the sample coordinate axes, (ii) the sample directions of maximum and minimum Young's modulus, and (iii) the trends with texture sharpening. The underlying reason is that these features are largely controlled by texture and not by material specific single-crystal elastic properties (this is true since $2S_{11} - 2S_{12} - S_{44} < 0$ for all the alloys, implying the same shape of the $E(\mathbf{n})$ and $T(\mathbf{n})$ surfaces). The specific single-crystal elastic properties of a material set the overall stiffness and elastic anisotropy. The latter determines the margin that texture effects can have. The impact of texture is the higher the larger is A_u , as seen for instance in the relative deviation of minimum and maximum Young's moduli from the isotropic value, E_{iso}^S , in Ti45Zr45Nb5Ta5, Ti37.5Zr25Ta12.5Hf12.5Nb12.5, and Ti40Zr10Nb30Ta10Fe10. Especially the latter alloy is rather elastically isotropic, and its minimum Young's modulus in textured aggregates can not be lowered significantly below the isotropic value.

5. Discussions

In this paper, the single-crystal elastic properties of 21 bcc RHEAs were investigated by DFT simulations and their polycrystalline elastic moduli were calculated adopting both random and non-random crystallographically textured distributions of grains. Characterizing the polycrystalline state by an ODF suffices for the present purpose and allows efficient and direct prediction of intrinsic elastic properties without the use of multi-scale modeling approaches [62]. For other purposes, for instance modeling the macroscopic plastic behavior, knowledge on other grain properties can be required in addition, e.g., properties associated with grain shape or misorientation between grains.

To compare the present results to other metallic implant materials and human bone, we summarize in Fig. 6 the calculated minimum single-crystal and polycrystalline Young's moduli for the

totality of 21 RHEAs examined in this paper. In calculating Young's modulus for the non-random textures shown in Fig. 6, a medium texture sharpness of 10° was used. The isoelastic Young's moduli E_{iso}^S of the RHEAs are below those of 316L stainless steel (≈ 210 GPa [2]) and Co-Cr-Mo alloy (≈ 240 GPa [2]). E_{iso}^S of some of the RHEAs are even lower than those of commercially pure Ti (≈ 100 GPa [2]) and Ti64 (≈ 110 GPa [2,63]). This indicates an improvement in biomechanical compatibility, even though the Young's moduli are still far above that of cortical bone (15–20 GPa; long-bone direction). As discussed above, the present theory overestimates E_{iso}^S systematically, suggesting that the isotropic Young's moduli of the RHEAs are lower (about 30% on average). For comparison, β -type Ti alloys show Young's moduli < 100 GPa, even as low as 55–60 GPa in some cases [63]. As RHEAs are a new material class, we anticipate that future work will discover new biocompatible RHEAs with significantly lower isotropic Young's modulus.

To address the fact that a load-bearing hip or knee prostheses practically receives the same, predominantly uniaxial loading pattern as the host bone, Section 4 explored two approaches to achieve a directionally preferential low Young's modulus, i.e., single crystals and crystallographic texture in polycrystalline materials. Clearly, single crystals offer the highest potential for reducing Young's modulus in certain crystal directions (Fig. 6). The relative lowering effect, $E(\langle 001 \rangle)/E_{iso}^S - 1$, predominantly scales with the single-crystal elastic anisotropy. As the elastic anisotropy of a polycrystal can not exceed that of the crystallites it is composed of, reducing Young's modulus in certain sample directions in textured polycrystals is generally less effective. Fig. 6 also shows that the lowering of Young's modulus is strongly dependent on the texture present. The SLM_C and SLM_G textures produce polycrystal aggregates that show “pseudo single crystal” elastic behavior due to the high degree of grain alignment, thus effectively exploit elastic anisotropy to reduce Young's modulus. This result is congruent with a previous experimental study for the β -type Ti-15Mo-5Zr-3Al alloy, in which a large anisotropy of Young's modulus was observed in SLM fabricated samples exhibiting a preferential orientation of columnar cells [46]. The two considered rolling textures are less beneficial in reducing Young's modulus in particular sample directions, but the effect is still pronounced in RHEAs with large A_u . The reason for why RT_x and RT_y are less effective is that neither the α -fiber nor the γ -fiber preferably align any of the low-modulus crystal directions (i.e., $\langle 001 \rangle$) along a particular sample direction. As with E_{iso}^S , the calculated minimum single-crystal

Table 6

Elastic anisotropy of Young's modulus $\langle E^S \rangle$ and $\overline{\langle T^S \rangle}(\theta_{\min}, \phi_{\min})$ in polycrystalline Ti37.5Zr25Ta12.5Hf12.5Nb12.5 possessing rolling-type texture or SLM-type texture for various texture sharpnesses represented by the half-width of the ODF kernel κ (the texture indexes t are identical to the ones in Table 4). The value of Young's modulus in special sample directions [(RD, TD, ND) or (XD, YD, BD)] is shown along with the minimum and maximum values across all directions with corresponding angles θ and ϕ . Among equivalent directions of minimum and maximum Young's moduli, only those with the lowest θ , then lowest ϕ are given. The moduli are in units of GPa and the angles in degree.

Rolling texture	κ	Anisotropy of Young's modulus $\langle E^S \rangle$									$\overline{\langle T^S \rangle}(\theta_{\min}, \phi_{\min})$
		RD	TD	ND	min	θ_{\min}	ϕ_{\min}	max	θ_{\max}	ϕ_{\max}	
RT_x	5°	132	124	126	111	48	28	132	90	0	46
	10°	129	123	125	112	48	28	129	90	0	46
	15°	127	122	123	113	48	29	127	90	0	46
RT_y	5°	131	130	155	104	47	25	155	0	0	48
	10°	129	128	149	106	47	26	149	0	0	48
	15°	126	126	140	109	48	27	140	0	0	47
SLM texture	κ	XD	YD	BD	min	θ_{\min}	ϕ_{\min}	max	θ_{\max}	ϕ_{\max}	$\overline{\langle T^S \rangle}(\theta_{\min}, \phi_{\min})$
SLM _C	5°	68	68	68	68	0	0	167	55	45	66
	10°	75	75	75	75	0	0	157	55	45	62
	15°	84	84	84	84	0	0	146	55	45	57
SLM _G	5°	68	122	122	68	45	90	167	35	0	66
	10°	75	123	123	75	45	90	157	35	0	62
	15°	84	123	123	84	45	90	146	35	0	57

Table 7

Elastic anisotropy of Young's modulus $\langle E^S \rangle$ and $\overline{\langle T^S \rangle}(\theta_{\min}, \phi_{\min})$ in poly-crystalline Ti40Zr10Nb30Ta10Fe10 possessing rolling-type texture or SLM-type texture for various texture sharpnesses represented by the half-width of the ODF kernel κ (the texture indexes t are identical to the ones in Table 4). The value of Young's modulus in special sample directions [(RD, TD, ND) or (XD, YD, BD)] is shown along with the minimum and maximum values across all directions with corresponding angles θ and ϕ . Among equivalent directions of minimum and maximum Young's moduli, only those with the lowest θ , then lowest ϕ are given. The moduli are in units of GPa and the angles in degree.

Rolling texture	κ	Anisotropy of Young's modulus $\langle E^S \rangle$			min	θ_{\min}	ϕ_{\min}	max	θ_{\max}	ϕ_{\max}	$\overline{\langle T^S \rangle}(\theta_{\min}, \phi_{\min})$
		RD	TD	ND							
RT _{α}	5°	143	142	142	139	49	30	143	90	0	54
	10°	143	141	142	139	49	30	143	90	0	54
	15°	142	141	141	139	49	30	142	90	0	53
RT _{γ}	5°	143	142	147	137	49	29	147	0	0	54
	10°	143	142	146	138	49	29	146	0	0	54
	15°	142	142	145	138	49	30	145	0	0	54
SLM texture	κ	XD	YD	BD	min	θ_{\min}	ϕ_{\min}	max	θ_{\max}	ϕ_{\max}	$\overline{\langle T^S \rangle}(\theta_{\min}, \phi_{\min})$
SLM _C	5°	128	128	128	128	0	0	149	55	45	57
	10°	130	130	130	130	0	0	148	55	45	57
	15°	132	132	132	132	0	0	146	55	45	56
SLM _G	5°	128	143	143	128	45	90	149	35	0	57
	10°	130	143	143	130	45	90	148	35	0	57
	15°	132	142	142	132	45	90	146	35	0	56

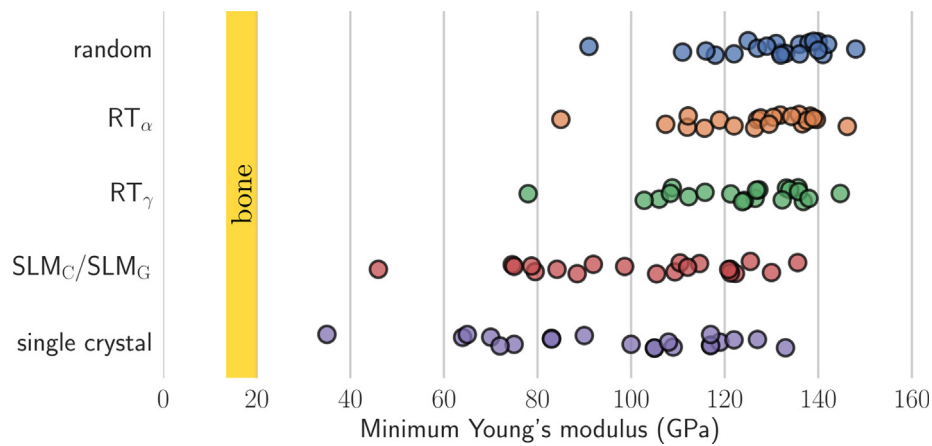


Fig. 6. For the present RHEAs, a higher single-crystal elastic anisotropy typically means a lower minimum Young's modulus. For comparison, the vertical yellow bar indicates the targeted Young's modulus of cortical bone.

and poly-crystalline Young's moduli contain errors. An assessment of the systematic and residual errors of $E(\langle 001 \rangle)$ is precluded by lack of experimental data. On the other hand, for textured polycrystals with large values of κ and/or those composed of crystals with small A_u , errors similar to those of E_{iso}^S are expected.

A fiber in bcc materials that does have its fiber axis oriented parallel to one of the $\langle 001 \rangle$ direction is the η -fiber (for rolling, e.g., $[100] \parallel \text{RD}$, from $(001)[100]$ to $(011)[100]$) [64]. The development of a strong η -fiber would be beneficial to reduce Young's modulus due to the preferable alignment of $\langle 001 \rangle$ crystal directions. However, the η -fiber forms less frequently than the common α and γ -fibers, although it was recently observed in a cold-groove-rolled β -type Ti alloy [45].

For the present RHEAs, a higher single-crystal elastic anisotropy roughly translates into a lower minimum Young's modulus, which is due to the fact that both properties show correlations with the VEC. The current results thus provide further evidence that the VEC has a dominant influence on the elastic properties of bcc alloys composed of mainly refractory elements and VEC between approximately 4 and 5 [65,66,21].

During walking and running, torsional loading, in addition to compression, is a common loading pattern in human tibia [67]. For torsion load on the long-bone axis, human cortical bone has a torsion modulus of 3–6 GPa [68,7]. To compare to the present

theoretical results, we considered the equivalent case when the torque axis is placed parallel to the (crystal or sample) direction of minimum Young's modulus. Then, our study firstly shows that the single crystal and poly-crystal torsion moduli in the RHEAs are roughly a factor of 10 to 20 larger than that of bone. Secondly, a low mismatch of Young's modulus and a low mismatch of the torsion modulus can not be simultaneously achieved in the alloys' single crystals and their poly-crystals with high texture index. This is not restricted to the presently considered alloys, but fundamentally related to the opposite direction dependences of E and T in bcc single crystals.

6. Conclusions

We presented a theoretical investigation of 21 biocompatible RHEAs, with current research mainly focused on Young's modulus and secondarily on the torsion modulus. The present theory predicted the lattice parameters and single-crystal elastic properties of the RHEAs in bcc structure and examined their poly-crystalline elastic moduli adopting both random and non-random orientation distributions. The present experiments synthesized four of these 21 RHEAs and measured their lattice parameters, quasi-isotropic Young's moduli, and Vickers hardnesses. Based on the theoretical

results and discussions presented, and supported by the obtained experimental Young's moduli, we mainly conclude that:

1. In randomly textured poly-crystals of the alloys, the theoretical Young's moduli (91–148 GPa) indicate an improvement in biomechanical compatibility with respect to surgical 316L stainless steel, Co-Cr-Mo alloy, and, for few of the alloys, Ti64 and commercially pure Ti.
2. In non-randomly textured poly-crystals of the alloys, the lowering of Young's modulus in certain sample directions starkly depends on the alignment of low-modulus crystal directions across grains. The α -fiber and γ -fiber are weakly to moderately effective in lowering Young's modulus, while distinct cube or Goss orientations have strong lowering potential depending on the control of texture sharpness.
3. In the alloys' single crystals, the Young's moduli and the torsion moduli are the lowest and the highest, respectively, in the directions of the cube axes $\langle 001 \rangle$, and vice versa in the $\langle 111 \rangle$ directions. Elastic anisotropy thus can not be exploited to achieve a low Young's modulus and a low torsion modulus in the same direction.
4. The VEC has a dominant influence on several alloying trends including elastic anisotropy, the single-crystal $E(\langle 001 \rangle)$ and $T(\langle 111 \rangle)$, and the poly-crystal E_{iso}^S and T_{iso}^S .

Overall, in this paper we demonstrated the potential of harnessing elastic anisotropy of single crystals and textured poly-crystals with the target to reduce Young's modulus. This strategy is applicable to other bcc materials with similar scope of application including β -type Ti alloys. As anisotropy can have important influences on other mechanical properties, for instance, yield stress, fracture toughness and formability, the benefit of anisotropy for the design of RHEAs for implant applications deserves further investigation.

Data availability

The data that support the findings of this study are available within the article.

Declaration of Competing Interest

The authors declare that they have no known competing financial interests or personal relationships that could have appeared to influence the work reported in this paper.

Acknowledgments

The Swedish Research Council [Grant Nos. 2017–06474, 2019–04971, and 2020–03736], the Swedish Steel Producers' Association, the Swedish Foundation for Strategic Research, the Swedish Energy Agency, the Carl Tryggers Foundation for Scientific Research [Grant No. 19:325], and the Hungarian Scientific Research Fund OTKA [Grant No. 109570] are acknowledged for financial support. X.-Q. Li also thanks the Göran Gustafsson Foundation [Grant No. 2121]. This work is partly supported by Grant-in-Aid for Scientific Research from the Japan Society for the Promotion of Science (JSPS) KAKENHI [Grant No. 19K14838]. The computations were performed on resources provided by the Swedish National Infrastructure for Computing (SNIC) at the National Supercomputer Centre in Linköping partially funded by the Swedish Research Council through Grant No. 2018–05973.

References

- [1] M. Long, H. Rack, Review: Titanium alloys in total joint replacement: a materials science, *Biomaterials* 19 (2006) 1621–1639.
- [2] M. Geetha, A. Singh, R. Asokamani, A. Gogia, Ti based biomaterials, the ultimate choice for orthopaedic implants—a review, *Prog. Mater. Sci.* 54 (2009) 397–425.
- [3] M. Saini, Y. Singh, P. Arora, V. Arora, K. Jain, Implant biomaterials: a comprehensive review, *World J. Clin. Cases.* 3 (2009) 52–57.
- [4] M. Niinomi, M. Nakai, J. Hieda, Development of new metallic alloys for biomedical applications, *Acta Biomater.* 8 (2012) 3888–3903.
- [5] R. Huiskes, H. Weinans, B. van Rietbergen, The relationship between stress shielding and bone resorption around total hip stems and the effects of flexible materials, *Clin. Orthop. Relat. Res.* 274 (1992) 124–134.
- [6] M. Niinomi, Recent research and development in titanium alloys for biomedical applications and healthcare goods, *Sci. Tech. Adv. Mater.* 4 (2003) 445–454.
- [7] M. Mirzaali, J. Schwiedrzik, S. Thaiwichai, J. Best, J. Michler, P. Zysset, U. Wolfram, Mechanical properties of cortical bone and their relationships with age, gender, composition and microindentation properties in the elderly, *Bone* 93 (2016) 196–211.
- [8] E.F. Morgan, G.U. Unnikrisnan, A.I. Hussein, Bone mechanical properties in healthy and diseased states, *Annu. Rev. Biomed. Eng.* 20 (2018) 119–143, <https://doi.org/10.1146/annurev-bioeng-062117-121139>.
- [9] M. Todai, T. Nagase, T. Hori, A. Matsugaki, A. Sekita, T. Nakano, Novel TiNbTaZrMo high-entropy alloys for metallic biomaterials, *Scr. Mater.* 129 (2017) 65–68.
- [10] T. Nagase, M. Todai, T. Hori, T. Nakano, Microstructure of equiatomic and nonequiatomic Ti-Nb-Ta-Zr-Mo high-entropy alloys for metallic biomaterials, *J. Alloy. Comp.* 753 (2018) 412–421.
- [11] G. Popescu, B. Ghiban, C. Popescu, L. Rosu, R. Trusca, I. Carcea, V. Soare, D. Dumitrescu, I. Constantin, M. Olaru, B. Carlan, New TiZrNbTaFe high entropy alloy used for medical applications, *IOP Conf. Series* 400 (2018) 022049.
- [12] T. Hori, T. Nagase, M. Todai, A. Matsugaki, T. Nakano, Development of nonequiatomic Ti-Nb-Ta-Zr-Mo high-entropy alloys for metallic biomaterials, *Scr. Mater.* 172 (2019) 83–87.
- [13] A. Motalebzadeh, N. Peighambarpour, S. Sheikh, H. Murakami, S. Guo, D. Canadine, Microstructural, mechanical and electrochemical characterization of TiZrTaHfNb and Ti1.5ZrTa0.5Hf0.5Nb0.5 refractory high-entropy alloys for biomedical applications, *Intermetallics* 113 (2019) 106572.
- [14] Y. Yuan, Y. Wu, Z. Yang, X. Liang, Z. Lei, H. Huang, H. Wang, X. Liu, K. An, W. Wu, Z. Lu, Formation, structure and properties of biocompatible TiZrHfNbTa high-entropy alloys, *Mater. Res. Lett.* 7 (2019) 225–231.
- [15] W. Yang, Y. Liu, S. Pang, P.K. Liaw, T. Zhang, Bio-corrosion behavior and in vitro biocompatibility of equimolar TiZrHfNbTa high-entropy alloy, *Intermetallics* 124 (2020) 106845.
- [16] G. Perumal, H.S. Grewal, M. Pole, L.V.K. Reddy, S. Mukherjee, H. Singh, G. Manivasagam, H.S. Arora, Enhanced biocorrosion resistance and cellular response of a dualphase high entropy alloy through reduced elemental heterogeneity, *ACS Appl. Bio Mater.* 3 (2020) 1233–1244.
- [17] T. Nagase, Y. Iijima, A. Matsugaki, K. Ameyama, T. Nakano, Design and fabrication of Ti-Zr-Hf-Cr-Mo and Ti-Zr-Hf-Co-Cr-Mo high-entropy alloys as metallic biomaterials, *Mater. Sci. Eng. C* 107 (2020) 110322.
- [18] Y. Iijima, T. Nagase, A. Matsugaki, P. Wang, K. Ameyama, T. Nakano, Design and development of Ti-Zr-Hf-Nb-Ta-Mo high-entropy alloys for metallic biomaterials, *Mater. Des.* 202 (2021) 109548, <https://doi.org/10.1016/j.matdes.2021.109548>. URL <https://www.sciencedirect.com/science/article/pii/S0264127521001015>.
- [19] S.G. Steinemann, Evaluation of Biomaterials, Wiley, 1980, Ch. Corrosion of surgical implants - in vivo and in vitro tests, pp. 1–34.
- [20] S.G. Steinemann, Metallurgy and Technology of Practical Titanium alloys, The Minerals, Metals and Materials Society, 1994, Ch. Effect of alloying elements on corrosion resistance of titanium alloys for medical implants, pp. 313–321.
- [21] M. Tane, S. Akita, T. Nakano, K. Hagihara, Y. Umakoshi, M. Niinomi, H. Nakajima, Peculiar elastic behavior of Ti-Nb-Ta-Zr single crystals, *Acta Mater.* 56 (2008) 2856–2863.
- [22] S. Lee, M. Todai, M. Tane, K. Hagihara, H. Nakajima, T. Nakano, Biocompatible low Young's modulus achieved by strong crystallographic elastic anisotropy in Ti-15Mo-5Zr-3Al alloy single crystal, *J. Mech. Behav. Biomed. Mater.* 14 (2012) 48–54.
- [23] U.F. Kocks, C.N. Tomé, H.-R. Wenk, Texture and Anisotropy, Preferred Orientations in Polycrystals and their Effect on Materials Properties, Cambridge University Press, Cambridge, 2000.
- [24] H. Wenk, P. Houtte, Texture and anisotropy, *Rep. Prog. Phys.* 67 (2004) 1367–1428.
- [25] J.F. Nye, Physical Properties of Crystals: Their Representation by Tensors and Matrices, Oxford University Press, New York, 1960.
- [26] R. Hearmon, The elastic constants of anisotropic materials, *Rev. Mod. Phys.* 18 (1946) 409–440.
- [27] K. Knowles, P.R. Howie, The directional dependence of elastic stiffness and compliance shear coefficients and shear moduli in cubic materials, *J. Elast.* 120 (2015) 87–108.
- [28] S.I. Ranganathan, M.O. Starzewski, Universal elastic anisotropy index, *Phys. Rev. Lett.* 101 (2008) 055504.
- [29] H.-J. Bunge, Texture Analysis in Materials Science, Butterworth & Co, 1982.

- [30] P. Van Houtte, L. De Buyser, The influence of crystallographic texture on diffraction measurements of residual stress, *Acta Metall. Mater.* 41 (2) (1993) 323–336.
- [31] J. Turlay, G. Sines, The anisotropy of Young's modulus, shear modulus and Poisson's ratio in cubic materials, *J. Phys. D: Appl. Phys.* 4 (1971) 264–272.
- [32] R. Hill, The elastic behaviour of a crystalline aggregate, *Proc. phy. Soc. A* 65 (1952) 349–354.
- [33] V.L. Moruzzi, J.F. Janak, K. Schwarz, Local density theory of metallic cohesion, *Phys. Rev. B* 37 (1988) 790.
- [34] X. Li, H. Zhang, S. Lu, W. Li, J. Zhao, B. Johansson, L. Vitos, Elastic properties of vanadium-based alloys from first-principles theory, *Phys. Rev. B* 86 (2012) 014105.
- [35] R. Hielscher, H. Schaeben, A novel pole figure inversion method: specification of the MTEX algorithm, *J. Appl. Cryst.* (2008), <https://doi.org/10.1107/S0021889808030112>.
- [36] D. Mainprice, R. Hielscher, H. Schaeben, Calculating anisotropic physical properties from texture data using the MTEX open source package, in: D.J. Prior, E.H. Rutter, D.J. Tatham (Eds.), *Deformation Mechanism, Rheology & Tectonics: Microstructures, Mechanics & Anisotropy*, Vol. 360, Geological Society, London, Special Publications, 2011, pp. 175–192. doi:10.1144/SP360.10.
- [37] O.K. Andersen, O. Jepsen, G. Krier, *Lectures on Methods of Electronic Structure Calculations*, World Scientific, Singapore, 1994, Ch. Exact Muffin-Tin Theory, pp. 63–124.
- [38] L. Vitos, H.L. Skriver, B. Johansson, J. Kollár, Application of the exact muffin-tin orbitals theory: the spherical cell approximation, *Comput. Mater. Sci.* 18 (2000) 24–28.
- [39] J.P. Perdew, Y. Wang, Accurate and simple analytic representation of the electron-gas correlation energy, *Phys. Rev. B* 45 (1992) 13244.
- [40] B.L. Gyorffy, Coherent-potential approximation for a nonoverlapping-muffin-tin-potential model of random substitutional alloys, *Phys. Rev. B* 5 (1972) 2382–2384.
- [41] L. Vitos, I.A. Abrikosov, B. Johansson, Anisotropic lattice distortions in random alloys from first-principles theory, *Phys. Rev. Lett.* 87 (2001) 156401.
- [42] L. Vitos, *Computational Quantum Mechanics for Materials Engineers*, Springer-Verlag, London, 2007.
- [43] H. Kim, T. Sasaki, K. Okutsu, J. Kim, T. Inamura, H. Hosoda, S. Miyazaki, Texture and shape memory behavior of Ti-22Nb-6Ta alloy, *Acta Mater.* 54 (2) (2006) 423–433, <https://doi.org/10.1016/j.actamat.2005.09.014>. URL <http://www.sciencedirect.com/science/article/pii/S1359645405005392>.
- [44] H. Matsumoto, S. Watanabe, S. Hanada, Microstructures and mechanical properties of metastable β TiNbSn alloys cold rolled and heat treated, *J. Alloys Compd.* 439 (1) (2007) 146–155, <https://doi.org/10.1016/j.jallcom.2006.08.267>. URL <http://www.sciencedirect.com/science/article/pii/S0925838806013570>.
- [45] Y. Shinohara, Y. Matsumoto, M. Tahara, H. Hosoda, T. Inamura, Development of (001) -fiber texture in cold-groove-rolled Ti-Mo-Al-Zr biomedical alloy, *Materialia* 1 (2018) 52–61, <https://doi.org/10.1016/j.mtla.2018.07.008>. URL <http://www.sciencedirect.com/science/article/pii/S2589152918300474>.
- [46] T. Ishimoto, K. Hagihara, K. Hisamoto, S.H. Sun, T. Nakano, Crystallographic texture control of beta-type Ti-15Mo-5Zr-3Al alloy by selective laser melting for the development of novel implants with a biocompatible low Young's modulus, *Scripta Mater.* 132 (2017) 34–38.
- [47] T. Nagase, T. Hori, M. Todai, S.H. Sun, T. Nakano, Additive manufacturing of dense components in beta-titanium alloys with crystallographic texture from a mixture of pure metallic element powders, *Mater. Des.* 173 (2019) 107771.
- [48] S.H. Sun, K. Hagihara, T. Nakano, Effect of scanning strategy on texture formation in Ni-25 at.%Mo alloys fabricated by selective laser melting, *Mater. Des.* 140 (2018) 307–316.
- [49] D. Raabe, K. Lücke, Rolling and annealing textures of bcc metals, *Mater. Sci. Forum* 157–162 (1994) 597–610.
- [50] B. Hutchinson, N. Hansen, P. van Houtte, D.J. Jensen, Deformation microstructures and textures in steels [and discussion], *Philos. Trans. R. Soc. A Math. Phys. Eng. Sci.* 357 (1756) (1999) 1471–1485. URL <http://www.jstor.org/stable/55196>
- [51] L.A.I. Kestens, H. Pirgazi, Texture formation in metal alloys with cubic crystal structures, *Mater. Sci. Technol.* 32 (13) (2016) 1303–1315, <https://doi.org/10.1080/02670836.2016.1231746>.
- [52] O. Senkov, S. Semiatin, Microstructure and properties of a refractory high-entropy alloy after cold working, *J. Alloys Compd.* 649 (2015) 1110–1123, <https://doi.org/10.1016/j.jallcom.2015.07.209>. URL <http://www.sciencedirect.com/science/article/pii/S0925838815306071>.
- [53] R. Eleti, V. Raju, M. Veerasham, S. Reddy, P. Bhattacharjee, Influence of strain on the formation of cold-rolling and grain growth textures of an equiatomic HfZrTiTaNb refractory high entropy alloy, *Mater. Charact.* 136 (2018) 286–292.
- [54] J.M. Wills, O. Eriksson, P. Söderlind, A.M. Boring, Trends in the elastic constants of cubic transition metals, *Phys. Rev. Lett.* 68 (1992) 2802.
- [55] P. Söderlind, O. Eriksson, J.M. Wills, A.M. Boring, Theory of elastic constants of cubic transition metals and alloys, *Phys. Rev. B* 48 (1993) 5844.
- [56] N. Al-Zoubi, S. Schönecker, X. Li, W. Li, B. Johansson, L. Vitos, Elastic properties of 4d transition metal alloys: Values and trends, *Comp. Mater. Sci.* 159 (2019) 273–280.
- [57] H.M. Ledbetter, Ratio of the shear and Young's moduli for polycrystalline metallic elements, *Mater. Sci. Engin.* 27 (1977) 133–136.
- [58] K. Lejaeghere, V.V. Speybroeck, G.V. Oost, S. Cottenier, Error estimates for solid-state density-functional theory predictions: An overview by means of the ground-state elemental crystals, *Crit. Rev. Solid State Mater. Sci.* 39 (2014) 1–24.
- [59] L. Tian, G. Wang, J.S. Harris, D.L. Irving, J. Zhao, L. Vitos, Alloying effect on the elastic properties of refractory high-entropy alloys, *Materials & Design* 114 (2017) 243–252.
- [60] F.H. Featherston, J.R. Neighbours, Elastic constants of tantalum, tungsten, and molybdenum, *Phys. Rev.* 130 (1963) 1324–1333, <https://doi.org/10.1103/PhysRev.130.1324>.
- [61] D.I. Bolef, R.E. Smith, J.G. Miller, Elastic properties of vanadium. I. Temperature dependence of the elastic constants and the thermal expansion, *Phys. Rev. B* 3 (1971) 4100–4108, <https://doi.org/10.1103/PhysRevB.3.4100>.
- [62] M. Diehl, J. Niehuesbernd, E. Bruder, Quantifying the contribution of crystallographic texture and grain morphology on the elastic and plastic anisotropy of bcc steel, *Metals* 9 (2019) 1252, <https://doi.org/10.3390/met9121252>.
- [63] L. Zhang, L. Chen, A review on biomedical titanium alloys: Recent progress and prospect, *Adv. Eng. Mater.* 21 (2019) 1801215.
- [64] M. Hölscher, D. Raabe, K. Lücke, Rolling and recrystallization textures of bcc steels, *Steel Res.* 62 (1991) 567–575.
- [65] E.S. Fisher, D. Dever, Relation of the c' prime elastic modulus to stability of b.c.c. transition metals, *Acta Metall.* 18 (1970) 265–269.
- [66] H. Matsumoto, S. Watanabe, N. Masahashi, S. Hanada, Composition dependence of Young's modulus in Ti-V, Ti-Nb, and Ti-V-Sn alloys, *Metall. Mater. Trans. A* 37 (2006) 3239–3249.
- [67] P. Yang, M. Sanno, B. Ganse, T. Koy, G. Brüggemann, L. Müller, J. Rittweger, Torsion and antero-posterior bending in the in vivo human tibia loading regimes during walking and running, *PLoS ONE* 9 (2014) e94525.
- [68] D.T. Reilly, A.H. Burstein, The elastic and ultimate properties of compact bone tissue, *J. Biomech.* 8 (1975) 393–405.